A VALIDATION OF THE VIIRS FAST RADIATIVE TRANSFER MODEL VIA BRIGHTNESS TEMPERATURE ANALYSIS IN LONGWAVE INFRARED CHANNELS

A Thesis

by

REBECCA LYNN EVRARD

Submitted to the Office of Graduate and Professional Studies of
Texas A&M University
in partial fulfillment of the requirement for the degree of

MASTER OF SCIENCE

Chair of Committee,	Ping Yang
Co-Chair of Committee,	Kenneth Bowman
Committee Member,	Anthony Filippi
Head of Department,	Ping Yang

August 2016

Major Subject: Atmospheric Sciences

ABSTRACT

Clouds cover at least two thirds of the Earth at any given time. Clouds play a large role in the Earth's global energy budget, but the impact of cirrus clouds is still widely questioned and researched. Cirrus clouds reside high in the atmosphere where temperatures are so cold that the cloud particles are comprised of ice crystals rather than water droplets. Gaining a better understanding of ice cloud optical properties and the distribution of cirrus clouds provides an explanation for the contribution of cirrus clouds to the global energy budget.

Using remote sensing techniques in conjunction with radiative transfer models (RTMs), accurate simulations of cirrus clouds can enhance the understanding of the global energy budget as well as improve the use of global climate models. Prior to their use, RTMs must be tested for accuracy and sensitivity to various cloud optical property (COP) pairs. A well validated RTM such as the Line-By-Line Radiative Transfer Model plus the Discrete Ordinates Radiative Transfer Program (LBLRTM + DISORT) is compared to a newer, faster RTM such as the Visible Infrared Imager Radiometer Suite (VIIRS) Fast Radiative Transfer Model (VFRTM). By comparing brightness temperature (BT) simulations from both models, the accuracy of the VFRTM can be obtained. Based on previous studies, a root mean square error (RMSE) < 0.5 K for brightness temperature difference (BTD) analysis is an appropriate level of error. This study shows RMSE < 0.2 K for BTD using reanalysis data for atmospheric profiles rather than idealized profiles and updated ice particle habit information from the Moderate-resolution Imaging Spectroradiometer (MODIS)

Collection 6 (C6). At a higher resolution, the simulated results of the VFRTM are compared to the observations of VIIRS to further indicate the accuracy of the model for use on a global scale as well as to validate the use of MODIS C6 data. RMSE results for the given case study represent $< 1.5\%$ error from the VFRTM for all cases. The VFRTM is validated and is an appropriate RTM to use for global cloud retrievals to help improve and update the global energy budget and global climate models.

ACKNOWLEDGMENTS

I would like to thank my committee chair, Dr. Ping Yang, my co-chair, Dr. Kenneth Bowman, and my committee member Dr. Anthony Filippi, for their guidance throughout the completion of my classes and research during my time at Texas A&M University.

I would also like to thank the other members of Dr. Yang's and Dr. Bowman's research groups for their help with various parts of my project. I would like to express special thanks to Yifeng Ding who was an immense help to me from the beginning to the end of my project.

My time here in College Station was made even more special by all of my fellow graduate students who I am now proud to call friends. Thank you all so much for your friendship and support over the last couple of years.

Finally, I would like to extend my immense gratitude to my family and friends for their unconditional love, support, and encouragement over the years. Specifically, thank you to my father for introducing me to weather, to my mother for providing an eloquent example of what a woman in a STEM field should be, and to my sister for helping me strive to be a strong individual.

NOMENCLATURE

AVHRR	Advanced Very-high Resolution Radiometer
BT	Brightness Temperature
BTD	Brightness Temperature Difference
COP	Cloud Optical Properties
D_{eff}	Effective Particle Size
DISORT	Discrete Ordinates Radiative Transfer
FIRTM-AD	Fast Infrared Radiative Transfer Model Using the Adding Doubling Method
FRTM	Fast Radiative Transfer Model
HRTM	High-spectral-resolution Radiative Transfer Model
IPNG	Infrared Atmospheric Sounding Interferometer
IR	Infrared
JPSS	Joint Polar Satellite System
LBLRTM	Line-By-Line Radiative Transfer Model
LUT	Look Up Table
MERRA	Modern-Era Retrospective Analysis for Research and Applications
MODIS	Moderate-resolution Imaging Spectroradiometer
NPOESS	National Polar-orbiting Operational Environmental Satellite System

OLS	Operational Linescan System
RMS	Root Mean Square
RSB	Reflective Solar Bands
RTE	Radiative Transfer Equation
RTM	Radiative Transfer Model
SDR	Sensor Data Records
SeaWiFS	Sea-viewing Wide Field-of-view Sensor
SNPP	Suomi National Polar-orbiting Partnership
SRF	Spectral Response Functions
τ	Optical Thickness
TEB	Thermal Emissive Bands
VFRTM	VIIRS Fast Radiative Transfer Model
VIIRS	Visible Infrared Imager Radiometer Suite

TABLE OF CONTENTS

LIST OF FIGURES

LIST OF TABLES

1 INTRODUCTION

1.1 Background

At any point in time, on average, two thirds of the Earth experiences cloud cover, and with the inclusion of sub-visible cirrus clouds, this number increases to nearly 73% (Stubenrauch et al., 2013). Though globally distributed, clouds are more prevalent over ocean than land, with cirrus clouds, in particular, found at all latitudes with no regard to season or land cover (Fu and Liou, 1993). On a global scale, cirrus accounts for 20-30% of all cloud cover, but in the tropics where they are the most prevalent, that number increases to at least 60-70% (Fu and Liou, 1993; Meyer, 2004; Baran, 2009). Cirrus clouds form high in the troposphere and have been known to extend into the lower stratosphere as well (Figure 1.1). With temperatures at the tropopause colder than -50°C, cirrus clouds

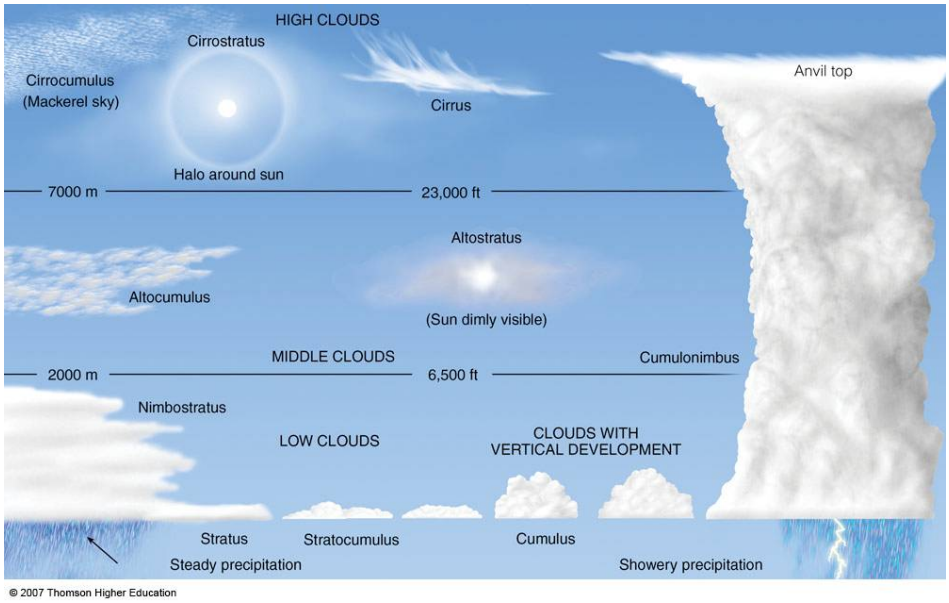

Figure 1.1: Cloud types (Ahrens and Samson, 2011)

are made up almost exclusively of non-spherical ice crystals of various shapes, sizes, and roughnesses. Magono and Lee (1966) were the first to comprehensively describe and classify ice crystals by updating work done by Nakaya (1954) with appropriate temperature and vapor conditions. More recently, work done by Baumgardner et al. (2005) and Baran (2009) show via in-situ measurements using optical particle spectrometers and a Cloud Particle Imaging probe respectively, that hexagonal columns, plates, and bullet-rosettes are the most common ice crystal habits found within cirrus clouds. Their findings matched those of Hobbs et al. (1975) who also found cirrus clouds to be comprised of those same habits 30 years earlier. Examples of these shapes and their descriptions are found in Figure 1.2 (Cole, 2013).

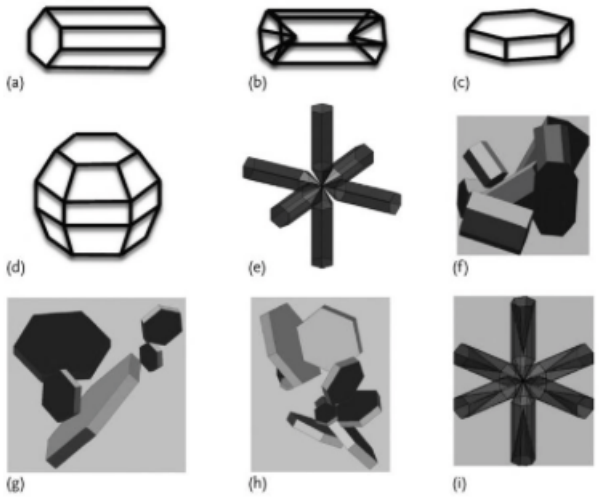

Figure 1.2: Common ice crystal habits: (a) solid column, (b) hollow column, (c) plate, (d) droxtal, (e) bullet rosette, (f) column aggregate, (g,h) plate aggregates, (i) hollow column rosette (Wendisch and Yang, 2012)

Cirrus cloud formation is primarily attributed to large-scale weather disturbances with different classifications of cirrus clouds being associated with specific weather pat-

terns. Low cirrus and cirrostratus are associated with high pressure systems or upper level troughs, while cirrus uncinus are related to mesoscale or synoptic scale disturbances. Extensive cirrus sheets are most often associated with frontal passages or anvil cloud remains. Work done by Yagi (1969) provides detailed synoptic conditions needed to form cirrus clouds, including stable air above and below the cloud layer as well as a dry adiabatic lapse rate and vertical wind shear at the top of the cloud. Yagi postulated that the static stability at the bottom of the cloud may be responsible for the shape and extent of the cirrus cloud.

Clouds play a large role in the Earth's global energy budget, but as shown in Figure 1.3, cloud types are not explicitly separated in global budgets. Weather and climate

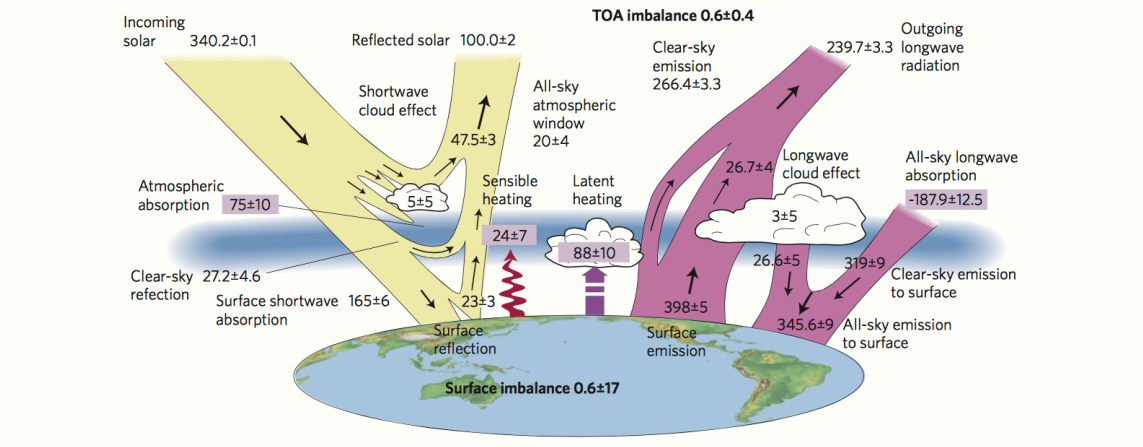

Figure 1.3: Global mean energy budget of Earth for 2000-2010 (Stephens et al., 2012)

on Earth depend on the distribution of incoming solar radiation from the sun, which may be scattered, reflected, or absorbed by clouds and aerosols in the atmosphere (Trenberth et al., 2009). Because cirrus clouds are high in the atmosphere, but can also be optically thin compared to lower, thicker clouds, they transmit almost all of the shortwave solar

radiation, but tend to trap longwave terrestrial radiation. This longwave radiation is absorbed and re-emitted, towards the Earth's surface, where some is absorbed and some is re-emitted creating a positive climate feedback loop that causes warming at the surface and in the troposphere (Liou and Takano, 1993). An example schematic in Figure 1.4 shows an example of this feedback loop. Due to the extensive spatial and temporal persistence of

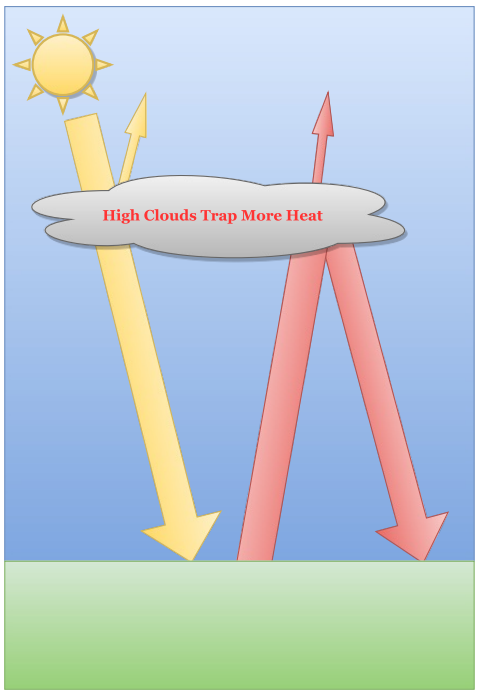

Figure 1.4: Positive climate feedback from high cirrus clouds

cirrus clouds, it is imperative to understand the radiative properties of these clouds (Meyer, 2004). Given the distribution of crystal shape, size, and roughness, deductions can be made about single-scattering properties such as the phase function, albedo, and extinction coefficient of a given ice particle. Any change in cloud microphysics can greatly affect the radiative properties and thus the radiative forcing of cirrus clouds. Liou (1986) found that ice crystal size distribution, assumed ice water content of a cloud, cloud thickness, and en-

vironmental conditions have a significant effect on the radiative forcing of cirrus clouds. Given the difficulty associated with obtaining an explicit ice crystal habit and radiative property information because of the high altitudes, optically thin nature, and non-spherical shape of ice crystals, the contribution of cirrus clouds to the Earth's global energy budget is still one of the most uncertain aspects of atmospheric science research. Having a better understanding of the spatial and temporal resolution of cirrus clouds through knowledge of their radiative properties could help improve the global energy budget and global climate models.

1.1.1 Remote Sensing

The International Satellite Cloud Climatology Project was one of the first field campaigns to facilitate in-situ cloud measurements to determine the spatial distribution and optical depth of cirrus clouds (Yang et al., 2014). Unfortunately, the aircraft-based measurements caused issues such as shattering the ice crystals as they were measured (Yang et al., 2014). Using LIDAR prevents ice crystal shattering and allows for the discrimination between water and ice clouds based on their backscatter signal. Given the various types of ice crystals contained within cirrus clouds, without a perfect knowledge of the scattering and polarization properties of each shape, LIDAR utilization unfortunately becomes more limited (Liou, 1986). Through various studies that predate the satellite era, it is made clear that a more cohesive and conclusive method of cirrus cloud detection is needed.

Remote sensing is "a method of obtaining information about properties of an object without coming into physical contact with that object" (Glickman, 2000). To infer the

physical and radiative properties of a remote object of interest, remote sensing uses the measurement of electromagnetic radiation based on passive (i.e., detects naturally occurring energy) or active (i.e., detects energy emitted from a sensor that reflects off a target) sensors on satellites, aircraft, or ground based systems (Yang et al., 2014). Unlike in-situ measurements that can destroy ice crystals and ground-based systems that have too much lower atmosphere interference, satellite remote sensing methods are the most practical choice for obtaining TOA measurements of the temporal and spatial properties of cirrus clouds.

Viewing cirrus clouds in the longwave (far) infrared (IR) portion of the electromagnetic spectrum (Figure 1.5) may hold the key to understanding the radiative effects of cirrus

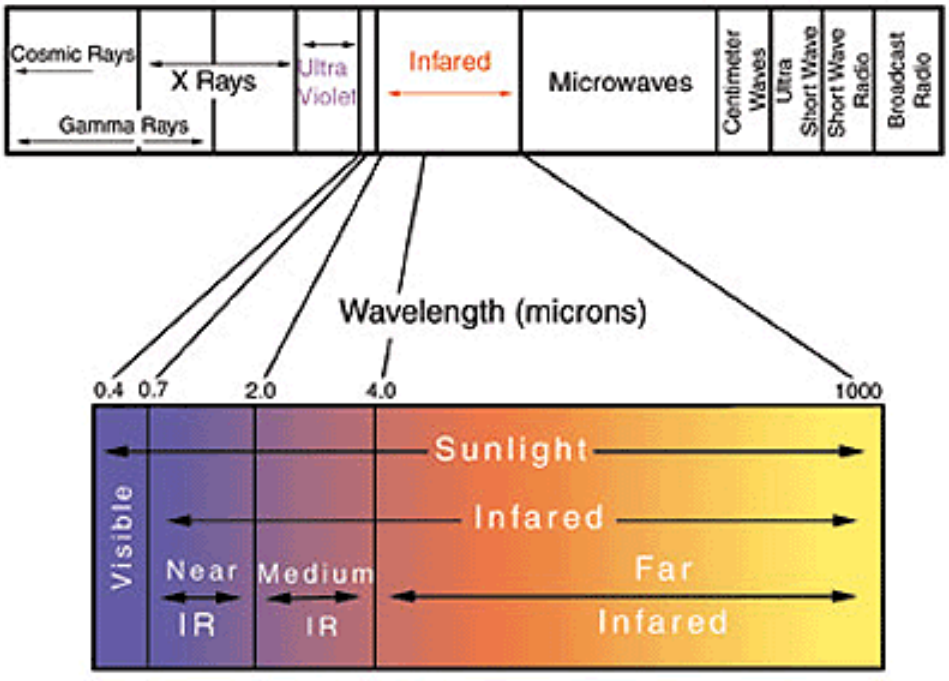

Figure 1.5: Electromagnetic spectrum (Lahti, cited 2016)

clouds. The best method for understanding the radiative effects of cirrus clouds is to ob-

tain and analyze the brightness temperatures (BT) or the measure of the amount of Top of Atmosphere (TOA) radiance in a given area. Formally, BT is "a descriptive measure of radiation in terms of the temperature of a hypothetical blackbody emitting an identical amount of radiation at the same wavelength," and is given by

$$BT = {B_\lambda}^{-1}[\varepsilon B_\lambda(T)] \tag{1.1}$$

where B_λ is Planck's law, ε is emissivity, and T is temperature (Glickman, 2000; Petty, 2006). When $\varepsilon = 1$, the BT is equal to the physical temperature of an object, and that object is considered to be a blackbody, which is a perfect absorber and emitter of incident radiation.

In the IR, a cloud-free atmosphere is transparent with little to no absorption or scattering. This allows solar radiation to pass unattenuated. When analyzing clouds however, the effect of absorption and emission in this region of the electromagnetic spectrum can be appreciable (Yang et al., 2001). Ice is highly absorptive and emissive in the IR. At larger optical thicknesses,cirrus clouds will act as blackbodies and emit radiation consistent with their temperatures. High, thick cirrus clouds exhibit the coldest BTs based on their altitude and temperature. High, thin cirrus clouds are not thick enough to act as blackbodies and instead transmit solar and terrestrial radiation through the cloud, giving BTs similar to the surface of the Earth. Thicker stratus or cumulus clouds found lower in the atmosphere have higher BT values, as they are representative of the temperatures lower in the atmosphere.

An understanding of the BT values of clouds of varying thickness and height can lead to insight into the radiative effects of various cloud types, especially cirrus. This could

ultimately be helpful for cloud retrievals. Using IR to analyze the properties of cirrus clouds has the additional advantage of greater consistency between daytime to nighttime viewing, and it is unaffected by sunglint from specular reflection off of the ocean surface, a common issue at visible wavelengths (Yang et al., 2001). Using IR wavelengths is also helpful for reducing the scattering effects of ice crystals. Phase functions, which describe the amount of angular distribution of energy scatter, become essentially featureless at IR wavelengths due to smoothing at side-scattering and back-scattering angles by absorption (Yang et al., 2001). Forward scattering can be removed via truncation techniques such as the delta-M method developed by Wiscombe (1977). These techniques are found in radiative transfer models.

1.1.2 Radiative Transfer

Remote sensing techniques are often paired with radiative transfer simulations. Radiative transfer is the theory that describes the propagation of radiation through a given medium that may have a combination of scattering, absorbing, or emitting objects. A radiative transfer model (RTM) is a computational description of the radiative transfer that produces radiation products for specific atmospheric conditions. RTMs aim to solve the complex radiative transfer equation (RTE) that accounts for the scattering, absorption, and emission of the atmosphere. The general RTE is given by

$$dI(\Omega) = -n\bar{\sigma}_{ABS}dxI(\Omega) - n\bar{\sigma}_{SCAT}dx\int_{4\pi}\frac{d\Omega'}{4\pi}p(\Omega',\Omega)I(\Omega) + n\bar{\sigma}_{ABS}dxB(T) + n\bar{\sigma}_{SCAT}dx\int_{4\pi}\frac{d\Omega'}{4\pi}p(\Omega,\Omega')I(\Omega') \quad (1.2)$$

where dx is an infinitesimal length, I is radiance, Ω is the direction of incident radiation, Ω' is the arbitrary direction for radiances, n is the number of objects per unit volume, $\bar{\sigma}_{ABS}$ is the average absorption cross section, $\bar{\sigma}_{SCAT}$ is the average total scattering, p is the scattering phase function, and $B(T)$ is the emission by a blackbody at the temperature of the object (Coakley and Yang, 2014). The left side of the equation represents a change in radiance as it passes through an infinitesimal volume of the atmosphere. The right side of the equation has four terms with the following meanings: radiance lost due to absorption in the volume, radiance lost due to scattering out of the direction of propagation, radiance gained due to emission within the volume, and radiance gained due to scattering in the direction of propagation (Coakley and Yang, 2014). A schematic of the processes from the general RTE can be seen in Figure 1.6. As ice clouds are highly absorptive and emissive

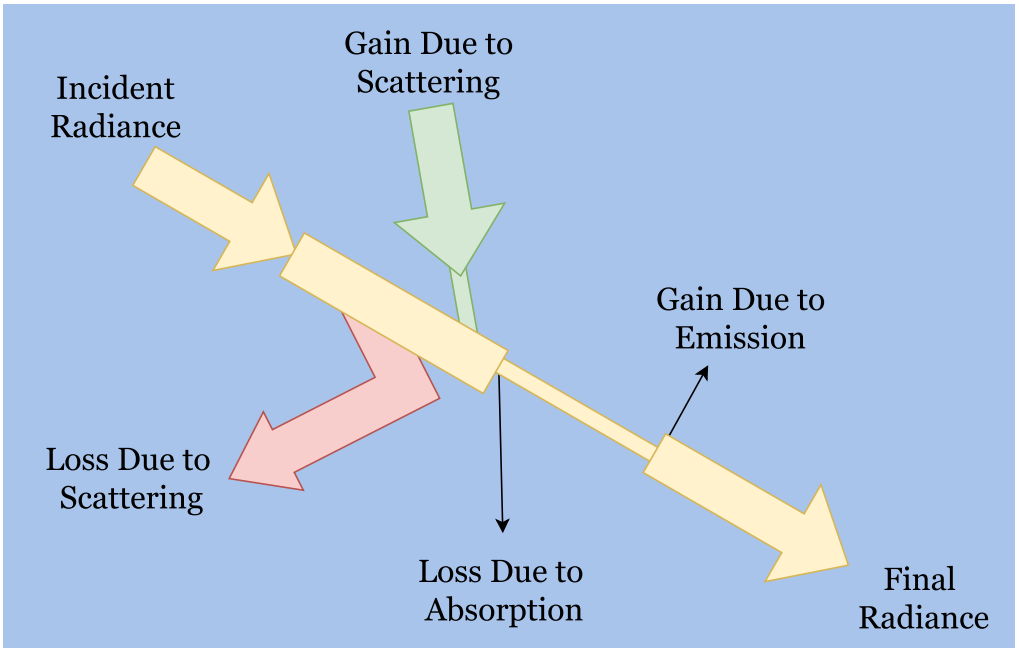

Figure 1.6: Illustration of a single beam of radiance and the processes that affect it as it propagates through space

but scattering is reduced at IR wavelengths, this equation can be simplified to fit the needs of the problem.

RTMs can be used to validate other RTMs or for retrieval of ice cloud properties. Retrieval of ice cloud properties is an inverse problem, or the conversion of radiometric or polarimetric measurements into physical properties (Yang et al., 2014). Validation is a direct problem where the ice cloud properties are assumed or are already known, and the radiometric or polarimetric measurements are simulated. By simulating and analyzing BT and brightness temperature difference (BTD), dependencies on optical thickness (τ) and effective diameter size (D_{eff}) arise and the accuracy of the RTM can be tested. Having an RTM that can be used for operational applications such as remote sensing data retrievals, cloud cover maps, or data assimilation is imperative. As older generation imagers are decommissioned, the need for newer RTMs optimized for use with the newest systems grows. The development of the Visible Infrared Imager Radiometer Suite (VIIRS) Fast Radiative Transfer Model (VFRTM) for use with the VIIRS sensor is further discussed below.

1.2 VIIRS Sensor

In 2010 the Joint Polar Satellite System (JPSS) was established as the next generation of polar-orbiting operational environmental satellite systems following a restructuring of the National Polar-orbiting Operational Environmental Satellite System (NPOESS) (Cao et al., 2013b). Prior to the reorganization of the program, NPOESS's key research ob-

jectives included conducting instrument risk reduction by offering early instrument and system-level testing, design modifications in a timely manner to ensure NPOESS launch readiness, and the reduction of risk to ground system processing including evaluating data products (Hutchison and Cracknell, 2005). JPSS continues to advance these research objectives.

The development and launch of the Suomi National Polar-orbiting Partnership (SNPP) satellite was the first mission for JPSS. The satellite is the namesake of Verner E. Suomi, a meteorologist from the University of Wisconsin who is widely recognized throughout the fields of Meteorology and Atmospheric Science as the "Father of Satellite Meteorology" (NOAA NESDIS JPSS, cited 2016). SNPP serves as the bridge between the old (i.e., Aqua and Terra) and new generations of NOAA and NASA satellite programs. SNPP was built by Ball Aerospace under a contract with Goddard Space Flight Center and is part of the Ball Configurable Platform family of satellites designed for cost-effective remote sensing use (NASA, cited 2016a). On board SNPP are five instruments: VIIRS, Cloud and Earth Radiant Energy System (CERES), Cross-track Infrared Sounder (CrIS), Advanced Technology Microwave Sounder (ATMS), and Ozone Mapping and Profiler Suite (OMPS) (NASA, 2011). With the addition of all of the instruments, SNPP has a payload of 2,100 kg and is the size of a small school bus (NASA, cited 2016a). Launched from Vandenberg Air Force Base, California on October 28, 2011 at 05:48 EDT, SNPP entered into an 824 km circular, sun-synchronous, polar orbit with a 13:30 local-time ascending node (NASA, cited 2016a, 2011). Orbiting the Earth from pole to pole about 14

times a day (period of 101.44 minutes), the entire surface of the Earth can be viewed twice a day (NASA, 2011).

Built by Raytheon, VIIRS is the largest instrument on SNPP (as show by Figure 1.7) weighing in at 275 kg (Raytheon Company, 2011). VIIRS is categorized as a whiskb-

Figure 1.7: SNPP spacecraft and instruments (SSEC University of Wisconsin-Madison, 2012)

room scanning radiometer that observes the Earth's surface in a cross-track direction with a scanning swath of $\pm 56^{\circ}$ by 3,040 km (Hutchison and Cracknell, 2005). It's development was based on a lineage of other satellites dating back to the 1970s. The Advanced Very-high Resolution Radiometer (AVHRR), the Moderate-resolution Imaging Spectroradiometer (MODIS), the Sea-viewing Wide Field-of-view Sensor (SeaWiFS), and the Operational Line-scan System (OLS) were the primary instruments from which inspiration was drawn for the design of VIIRS (Cao et al., 2013b). Raytheon wanted to develop a product that combined the radiometric accuracy of AVHRR with the high spatial resolution of OLS and

the success of MODIS (Raytheon Company, 2011). A rotating telescope (also found on SeaWiFS) and the addition of a day-night-band based on the OLS design were included in the final design of VIIRS (Cao et al., 2013b).

There are several improvements between VIIRS and its predecessors. The higher orbit of SNPP allows for full global coverage and better control of stray-light, which is detected light that is not from the bandwidth of the measuring wavelength due to light scattering, light diffraction, or instrument error (Cao et al., 2013b). VIIRS also uses "bow-tie removal" (i.e., scan-to-scan overlap in off-nadir areas which is not transmitted to the ground and is instead assigned a fill value) to save transmission bandwidth (Cao et al., 2013b). The "bow-tie effect" itself comes from the pixel growth rate (i.e., the growth of the sample distance due to increased distance between the ground and the sensor) increasing from 11.7 km at nadir to 25.8 km at the end of scan. Using pixel aggregation to control the pixel growth towards the end of a scan, VIIRS is able to improve (as much as 4 times) upon the pixel growth problem that exists for its predecessors AVHRR and MODIS (Cao et al., 2013b). This allows for the spatial resolution throughout the scan to be more comparable. According to Cao et al. (2013a), at a 375 m to 750 m spatial resolution (depending on the spectral band), the VIIRS thermal imaging bands have outperformed both MODIS and AVHRR, each of which has an IR resolution of 1 km (Cao et al., 2013a; Hillger et al., 2013). VIIRS was also created with the intent of lasting nearly twice as long as its predecessors (Raytheon Company, 2011).

There are 22 spectral bands covering the electromagnetic spectrum from 0.412 μm to

12.01 μm through the visible, near-IR, mid-IR, and long-wave-IR regions (Hutchison and Cracknell, 2005). More specifically, there are 16 moderate resolution bands (M-bands), five imaging resolution bands (I-bands), and one panchromatic day-night-band. The M-bands have 11 reflective solar bands (RSB) and five thermal emissive bands (TEB), and the I-bands have three RSBs and two TEBs (Cao et al., 2013b). The spectral bands themselves are comparable to those in MODIS, with most of the RSBs and some of the TEBs having wider to near double bandwidths, leading to better spatial resolution while maintaining the signal to noise ratio (SNR) (Cao et al., 2013b). Exact specifications including spatial resolution and wavelength range can be found in Figure 1.8. RSBs on VIIRS were turned on November 8, 2011, and the nadir door was opened November 21, 2011, marking the first day visible images were available (Cao et al., 2013b).

1.3 Radiative Transfer Models

There are a plethora of RTMs that are used to answer a multitude of radiative transfer problems. The LBLRTM + DISORT method is a well validated and highly accurate model. The results are used to compare to faster RTMs such as the VFRTM which is a newer model that must be validated for new data sets and conditions.

1.3.1 LBLRTM + DISORT

This model involves a combination of the Line-By-Line Radiative Transfer Model (LBLRTM) and the Discrete Ordinates Radiative Transfer FORTRAN90 Program (DISORT), referred to as LBLRTM + DISORT. Both LBLRTM and DISORT use a background

VIIRS Band	Central Wavelength (µm)	Wavelength Range (µm)	Band Explanation	Spatial Resolution (m) @ nadir
M1	0.412	0.402 - 0.422	Visible/ Reflective	750 m
M2	0.445	0.436 - 0.454		
M3	0.488	0.478 - 0.488		
M4	0.555	0.545 - 0.565		
M5 (B)	0.672	0.662 - 0.682		
M6	0.746	0.739 - 0.754	Near IR	
M7 (G)	0.865	0.846 - 0.885		
M8	1.240	1.23 - 1.25	Shortwave IR	
M9	1.378	1.371 - 1.386		
M10 (R)	1.61	1.58 - 1.64		
M11	2.25	2.23 - 2.28		
M12	3.7	3.61 - 3.79	Medium-wave IR	
M13	4.05	3.97 - 4.13		
M14	8.55	8.4 - 8.7	Longwave IR	
M15	10.763	10.26 - 11.26		
M16	12.013	11.54 - 12.49		
DNB	0.7	0.5 - 0.9	Visible/ Reflective	750 m across full scan
I1 (B)	0.64	0.6 - 0.68	Visible/Reflective	375 m
I2 (G)	0.865	0.85 - 0.88	Near IR	
I3 (R)	1.61	1.58 - 1.64	Shortwave IR	
I4	3.74	3.55 - 3.93	Medium-wave IR	
I5	11.45	10.5 - 12.4	Longwave IR	

M = Moderate (750 m) resolution bands
I = Imagery (375 m) resolution bands
DNB = Day-Night Band (or Near Constant Contrast (NCC) band)

M-bands highlighted in pale yellow are available as EDRs, in addition to SDRs.

Red, Green, and Blue components of true-color visible imagery are also highlighted.
True-color component bands are highlighted in red, green, and blue.
Natural-color component bands are noted with R, G, and B.

Figure 1.8: VIIRS bands (Hillger, cited 2016)

atmosphere that is plane parallel (i.e., horizontal variations are ignored and dependence on height is assumed), and vertically inhomogeneous divided into discrete homogeneous and isothermal atmospheric layers for clear sky with a vertically homogeneous but non-isothermal cloud able to be inserted an any level. LBLRTM is a line-by-line model developed and produced by Atmospheric and Environmental Research, Inc. LBLRTM is based on FASCODE (Fast Atmospheric Signature Code) developed at the Air Force Geophysics Laboratory to be a line-by-line calculation of radiance and transmittance of the atmosphere (Clough et al., 2005). LBLRTM uses a Voigt line shape and has an algorithmic accuracy

of calculation of approximately 0.5%, except in the wings of the Voigt lines where that error can increase to $\pm 3\%$ (Atmospheric and Environmental Research, cited 2016; Clough et al., 1981). LBLRTM is used to calculate gaseous absorption and transmittance over a spectrum with results used in both clear sky and cloudy sky cases. Gas transmittance is needed for further calculations in a thermal band RTM such as DISORT.

Disseminated by NASA's Goddard Space Flight Center and written by Stamnes et al. (1988), DISORT strives to be the most general RTM available to the public (Stamnes et al., 2000). The code was written to be a new implementation of the discrete ordinates method for vertically layered atmospheres (Stamnes et al., 1988). The discrete ordinates method for radiative transfer comes from the work of Chandrasekhar (1960) where the solution to the radiative transfer equation (RTE) is derived using a finite set of discrete-streams representing the angles in the integration. This method is therefore a numerical and approximate solution technique for solving the RTE and is reliable for radiative transfer calculations for atmospheres with clouds (Liou, 1973; Wendisch and Yang, 2012). According to Stamnes et al. (1988), the computation time of DISORT can be derived as the third power of the number of streams (i.e., direction in which radiation is propagating) used and becomes the most cumbersome portion of the computation time. Using double precision and the δ-M method, forward scattering is truncated in DISORT, and computational efficiency is increased slightly (Stamnes et al., 1988). By using both methods in conjunction, a high level of accuracy can be obtained, but in relation to other RTMs, computational efficiency is reduced. Using this method allows for a benchmark result to be obtained and later compared

to simulations from faster RTMs as a means of verifying the results of the faster models (e.g., VFRTM).

1.3.2 VFRTM

The VFRTM is a type of high-spectral-resolution forward RTM developed at Texas A&M University by Chenxi Wang in 2013. It was created to be a fast and computationally efficient RTM without loss of accuracy for a given satellite-based instrument with the purpose of advancing operational retrievals of atmospheric profiles and cloud or aerosol properties (Liu et al., 2014). The fast RTMs (FRTM) were initially developed for application to the Atmospheric Infrared Sounder, the Infrared Atmospheric Sounding Interferometer, MODIS, and Spinning Enhanced Visible and Infrared Imager instruments. The purpose of the VFRTM is to create a FRTM that can be optimized for the instruments of the future, such as VIIRS. During the transition period between MODIS and VIIRS data, the VFRTM can use data from either imager. In order to accurately simulate radiative transfer in the IR, an RTM must be able to calculate both gaseous absorption and multiple scattering within each cloud layer.

An efficient RTM used for the remote sensing of objects needs to have a clear-sky transmissivity or absorption τ simulator, a fast RTE solver, and a cloud multiple scattering model (Wang, 2013). Using correlated-k distribution (CKD) methods, gaseous absorption calculations are approximated rather than using the longer, tedious line-by-line method. Calculations use continuum absorption to account for gas absorption and treat H_2O, CO_2, and O_3 as a mixed gas instead of as separate constituents (Wang, 2013). H_2O, CO_2, and

O_3 are the three primary absorbers of the longwave IR atmospheric window seen in Figure 1.9 between 8 and 14 μm. The primary reason for including continuum absorption is the

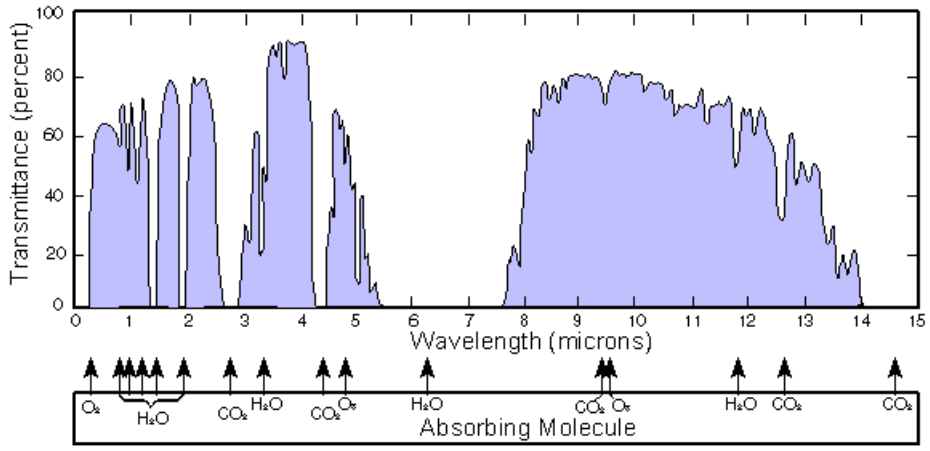

Figure 1.9: Transmittance and absorbing molecules of the atmospheric windows (US Navy, cited 2016)

importance of pressure broadened lines in the far wings, especially in the 700-1200 $cm^{-}1$ region where the bandwidths being used for this study are located (Clough et al., 1989). Once the transmissivities are calculated, they are put into look up tables (LUTs) for each VIIRS channel being studied. To further solve the problem of computational inefficiency, several studies (Baran and Francis, 2004; Wei et al., 2004; Dubuisson et al., 2005; Heidinger et al., 2006; Niu et al., 2007; Zhang et al., 2007; Wang et al., 2011) developed a series of fast RTE solvers to help facilitate ice cloud retrieval algorithms for single layer clouds (Wang et al., 2011). The RTE used in the VFRTM is the IR FRTM from Wang et al. (2011).

Finally, an ice cloud that is prone to multiple scattering needs to be added to the RTM. Using the example of Figure 1.10, there are $N-1$ layers in the atmosphere, with an

ice cloud layer at L_M. $T(z)$ gives the air temperature at an altitude z, τ_N is the optical depth

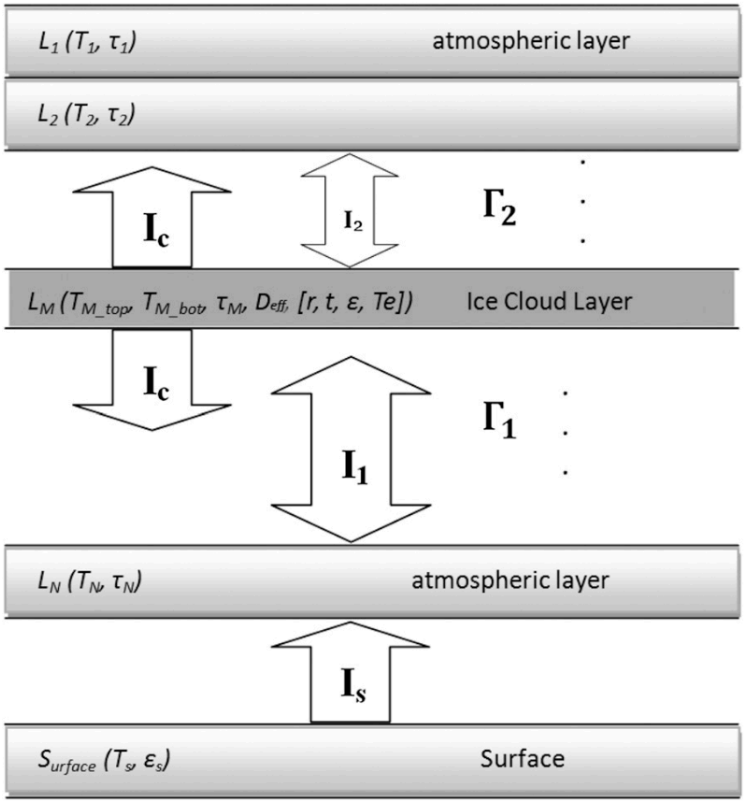

Figure 1.10: Example of a single ice cloud layer atmosphere (Wang et al., 2011)

of layer N, ε is the emissivity, I_N represents the emitted or reflected radiance from a layer N, and $\Gamma(z)$ represents the transmissivity of the atmosphere from the TOA to an altitude z (Wang, 2013). The sum of Equations 1.3, 1.4, and 1.5 yields I_{TOA}, which is necessary to analyze BT (Wang, 2013).

$$I_A = I_s\Gamma_1 t\Gamma_2 + I_1^{\uparrow} t\Gamma_2 + I_c^{\uparrow}\Gamma_2 + I_2^{\uparrow} \tag{1.3}$$

$$I_B = (I_1^{\downarrow} + I_c^{\downarrow}\Gamma_1 + I_2^{\downarrow} t\Gamma_1) \times (1-\varepsilon_s)\Gamma_1 t\Gamma_2 \tag{1.4}$$

$$I_C = I_2 t\Gamma_2 \tag{1.5}$$

In the above equations, the upward arrow represents up-welling radiances, and the down-

ward arrow represents down-welling radiances.

To account for the scattering within each layer, the VFRTM uses high-spectral-resolution ice cloud bulk scattering properties (Baum et al., 2007), single scattering properties of ice crystals (Yang et al., 2005; Zhang et al., 2004), and in-situ microphysical data (Wang, 2013). The ice cloud bulk scattering properties used to account for scattering within each layer were created using DISORT for 33 τ values ranging from 0.01 to 100, 18 D_{eff} values from 10 to 180 μm, nine viewing zenith angles from 0° to 180°, and 600 monochromatic wavenumbers with a 0.1 cm^{-1} from 700 cm^{-1} to 1300 cm^{-1} (Wang, 2013). The results are stored in LUTs and are called within the program for specific wavelengths.

1.4 Previous Studies

Starting with a study that predates the launch of VIIRS, this section aims to show the improvement of RTMs over the last 10 years with a focus on those with remote sensing applications and high-spectral-resolution results. All look at BT simulations in the IR spectrum as a means of validating the RTM in use against the slower but more accurate LBLRTM + DISORT. Using various methods of numerical and approximate solution techniques for solving the RTE, these studies provide a framework of reference for this study. Close attention is paid to RTM setups and data used as well as validation techniques and results.

1.4.1 Zhang et al., 2007

An important concept in the Zhang et al. (2007) study is that an RTM needs to be computationally efficient and accurate, as well as applicable to a variety of conditions. RTMs can be used to observe cloud clearing, for cloud optical property (COP) retrieval, and for satellite data assimilation. In general, multiple scattering makes solving the RTE difficult, but in the IR region that problem is simplified due to minimal scattering in the IR region of the electromagnetic spectrum. Previous RTM studies remove this feature of the RTE altogether which limits the flexibility of the model. Using methods such as DISORT or the Monte Carlo method, multiple scattering can be fully accounted for, providing a wide range of uses for the RTM. It is however, computationally inefficient to apply these methods to a broadband spectrum. By using modifications to the algorithms, efficiency is increased.

The fast infrared radiative transfer model (FIRTM-AD) was developed using the adding-doubling principle. Using a vertically inhomogeneous, multilayer, plane parallel atmosphere, the FIRTM-AD is a clear sky model that can also account for molecular absorption and an RTE solver that accounts for multiple scattering in cloud layers are developed. Pre-computed LUTs for reflection, transmission, and emissivity are calculated with appropriate COP and wavelengths. These LUTs help to save computational time and increase efficiency, but bring into question the reduction in accuracy due to necessary interpolation at some points. Clouds and atmospheric gases “coexist” within a single layer (rather than having gases in the atmosphere above and below the clouds) which results in

an increase of optical thickness and a decrease of single scattering albedo.

The accuracy of the FIRTM-AD is tested by computing BT across the spectrum at a high spectral resolution of 0.1 cm^{-1} and comparing the results to those from the DISORT model using the same conditions. A standard tropical atmospheric profile is divided into 100 layers over a 100 km atmospheric depth with a vertical resolution of 0.5 - 2.5 km. There is a single ice cloud layer around 14 km above the surface. BTs are simulated for both the FIRTM-AD and DISORT for various COP combinations and viewing angles, and the difference between the results is taken. The errors from previous RTMs that remove multiple scattering are represented by the root mean square (RMS) error of the BTD and are on the order of 0.5 K. The Noise Equivalent Differential Temperature of hyper-spectral sounders is 0.2 K. As the FIRTM-AD takes into account multiple scattering, and the hyper-spectral sounders have the lowest error level, the FIRTM-AD should also have error $<$ 0.2 K. Errors from FIRTM-AD are an order of magnitude smaller than the prescribed error level, with all results $<$ 0.05 K. This RTM is highly accurate and can be used for observational applications.

1.4.2 Wang et al., 2011

RTMs developed for scientific research such as DISORT, and those using the Monte Carlo method and adding-doubling techniques, are not optimal for use in operational applications such as satellite data products. The development of a fast RTM (FRTM) by Wang et al. (2011) that uses parametrizations (such as CKD) to minimize computational effort for high-spectral-radiance simulations, is helpful for operational needs. The background at-

mosphere used for simulations is plane parallel vertically inhomogeneous atmosphere and can be divided into discrete homogeneous and isothermal clear atmospheric layers with a vertically homogeneous but non-isothermal ice cloud inserted at an appropriate level. Molecular scattering under clear sky conditions is ignored here due to the lack of scattering in IR wavelengths, but the CKD method is used by the FRTM to derive atmospheric transmittance. For cloudy sky cases, bulk scattering is inferred from single scattering properties that are generated by DISORT and placed into LUTs.

Comparisons are made between the FRTM and LBLRTM + DISORT simulated BTs using a generalized tropical atmosphere broken down into 100 layers over a 100 km atmospheric depth with a vertical resolution of 0.5 - 2.5 km. For a zenith angle of 20° and $\tau <$ 5, the BTD is < 0.1 K and decreases to < 0.01 K for an increasing τ. This decrease is due to the opaque clouds acting as blackbodies. BTD values are also higher for smaller D_{eff}. There is a higher level of accuracy from the 12 μm channel, possibly due to the imaginary part of the ice refractive index increasing monotonically as a function of wavelength. This points to the importance of scattering for small ice particles, which causes large BTDs. This means that the FRTM may not handle scattering as well as DISORT. After obtaining error values that are sufficiently small enough, the FRTM can be used to infer ice cloud properties in satellite data using algorithms with COP chosen by low RMS error levels.

1.4.3 Wang et al., 2013

Based on similar work done in Wang et al. (2011), the Wang et al. (2013) study focuses on a need for an accurate and rapid thermal IR RTM that incorporates both gaseous

absorption and multiple scattering within cloud layers. LBLRTM accounts for line and continuum absorption while RTMs such as DISORT consider multiple scattering and create benchmark results. A high-spectral-resolution cloudy sky RTM (HRTM) was developed in this study to account for gaseous absorption based on the FRTM from Wang et al. (2011).

Wang et al. (2013) created the HRTM based on a fast clear sky transmittance simulator, a fast RTE solver, and an ice cloud multiple scattering thermal emission and absorption model. A clear sky transmission database is generated with a 0.1 cm^{-1} spatial resolution using pressure, temperature, and absorption profiles rather than using LBLRTM to derive them. Gases are treated as "mixed gases" in the database so that continuum absorption can be used to save computational effort. An RTE solver uses LUTs to account for multiple scattering, absorption, and thermal emissions within the cloud layer. Ice cloud bulk scattering products for high-spectral-resolution cases are developed from single scattering properties and in-situ micro-physical data.

Using a mid-latitude summer atmosphere broken into 70 layers for cloudy sky simulations, the HRTM BT simulations are compared to BT simulations from LBLRTM + DISORT. The largest error was 0.2 K for small COP pairs, and the largest error was found in areas of large absorption. With an increase in τ, RMS error reduces to 0.05 K due to the opacity of the cloud. These results show that the HRTM can model thin cirrus clouds and can be used further to infer COP from collocated observed data sets. Using a high-spectral-resolution application for the FRTM, this RTM is able to work with various other spectroradiometers that previous RTMs could not have handled well.

1.4.4 Liu et al., 2014

Using multiple streams, low orders of scattering, or LUTs as approximations, accuracy of the model is reduced, but computational efficiency is improved. The Liu et al. (2014) study develops an FRTM that uses CKD to minimize computation time and places an emphasis on simulating VIIRS data while allowing for application to other imagers. CKD was used as an approximation to LBLRTM techniques to calculate gaseous absorption by replacing the integral of gas transmission over highly variable spectral space with a smoother absorption coefficient space. This method also treated overlapping lines associated with different gases as one gas by combining absorption coefficients of multiple gases to reduce computation time. By creating a CKD model for each spectral channel associated with VIIRS, gaseous absorption could be calculated quickly for each channel. Transmissivities for the clear sky case were calculated using a US Standard Atmospheric Profile divided into 50 layers, each 1 km thick. The results were then used in the cloudy sky cases to simulate BT using the FRTM from Wang et al. (2011), along with bulk scattering properties and MODIS C6 data used for ice cloud properties. Results are averaged over the spectrum using spectral response functions (SRF).

When comparing the simulations of the FRTM to LBLRTM + DISORT, the BTD error was < 0.15 K, and it decreased to < 0.1 K for larger τ. Once the accuracy level of the FRTM was found to be high enough, a case study was done to assess the performance of the simulator. Atmospheric profiles from MERRA and COP from MODIS C6 were used to simulate BTs to compare to VIIRS observations. The simulation showed close agreement

to the VIIRS observations with differences due to error from model approximations and model assumptions, retrieved cloud properties, and atmospheric profiles. The last three error types account for the bulk of the discrepancies, showing that the model itself still has high performance accuracy for simulations.

2 DATA

For this validation study, VIIRS data granules are selected over ocean to remove land based biases and near the Intertropical Convergence Zone (ITCZ) where convection and therefore ice clouds are more likely to be found. After looking at the GOES-West satellite IR imagery for clouds and convection, the frame of temporal reference was reduced to two granules, a daytime granule on June 20, 2014 and a nighttime granule on June 21, 2014. The June 21, 2014 granule was tested first, with the June 20, 2014 granule selected at a later time to provide further validation. The exact temporal and spatial information for the areas being studied can be found in Figure 2.1.

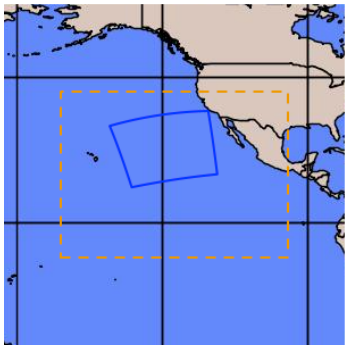

Temporal (Geographic Overlap):	
Start Date: 2014-06-20 22:07:51.000	**End Date:** 2014-06-20 22:13:32.000
Seconds: 341	**Direction:** Ascending
Spatial (Geographic Overlap):	
1. NW Lat,Long: 29.94 , -151.06	**2. NE Lat,Long:** 34.58 , -120.57
3. SW Lat,Long: 10.96 , -144.25	**4. SE Lat,Long:** 14.98 , -117.77

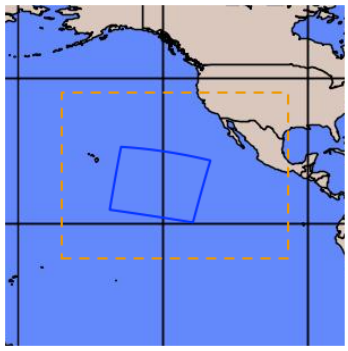

Temporal (Geographic Overlap):	
Start Date: 2014-06-21 10:38:57.000	**End Date:** 2014-06-21 10:44:37.000
Seconds: 340	**Direction:** Descending
Spatial (Geographic Overlap):	
1. NW Lat,Long: 23.76 , -147.78	**2. NE Lat,Long:** 19.54 , -120.03
3. SW Lat,Long: 4.29 , -151.28	**4. SE Lat,Long:** 0.37 , -125.45

Figure 2.1: Temporal and spatial information for granules (NOAA, cited 2016)

2.1 VIIRS

As the satellite orbits, VIIRS scans a swath of the Earth that is about 3,040 km wide in the cross-track direction (Seaman, 2013). A rotating mirror reflects radiation onto the 16 detectors of the M-bands, and each rotation is one scan that produces a strip of data 12 x 3,040 km in size (Seaman, 2013). One granule is constructed using 48 scans covering a combined area of 570 x 3,040 km in size (Seaman, 2013). The large granules distributed by the National Oceanic and Atmospheric Administration Comprehensive Large Array-data Stewardship System are actually four granules combined into one larger data set covering an area of 2,280 x 3,040 km (Seaman, 2013). The data is transmitted to the ground as raw data records which are processed, calibrated, and converted to Sensor Data Records (SDR) (Seaman, 2013). JPSS VIIRS Sensor Data Record (VIIRS_SDR) data sets contain the geolocation files, and BT information for the longwave IR channels (Seaman, 2013). The geolocation files contain latitude, longitude, surface elevation, satellite zenith angle, satellite azimuth angle, solar zenith angle, solar azimuth angle, and distance to satellite (Seaman, 2013). Additionally, the JPSS VIIRS Non-Gridded Intermediate Products (VIIRS_IPNG) data sets with the same temporal and spatial distribution as the SDR files are used in this study. VIIRS COP and cloud top parameters containing τ, D_{eff}, and cloud top height information are held in the VIIRS_IPNG data set.

2.2 MERRA

This study uses the Modern-Era Retrospective Analysis for Research and Applications (MERRA) to create atmospheric profiles as input for the RTMs. MERRA is a reanalysis of the atmosphere performed by NASA using the Goddard Earth Observing System Model Version 5 (NASA, cited 2016b). The files used in this study contain standard products (state variables) that are assimilated, meaning they use a combination of atmospheric data analysis and model forecasts to generate a series of global atmospheric quantities that are closer to the actual atmospheric state than idealized atmospheric profiles used in previous studies (Global Modeling and Assimilation Office, 2012). The frequency of data collection is every 3 hours (00, 03, 06, 09, 12, 15, 18, 21 UTC) (Global Modeling and Assimilation Office, 2012). Finally, the grid is reduced to a 1.25° x 1.25° horizontal spatial resolution with vertical pressure over 42 levels ranging from 1000 mb to 0.1 mb (Global Modeling and Assimilation Office, 2012). The MERRA product used are air temperature, ozone mixing ratio, geopotential height, and specific humidity (Global Modeling and Assimilation Office, 2012). An example of the four products used to create atmospheric profiles for each grid point in the area of the granule can be seen in Figure 2.2. 1,000 mb air temperatures are used in VFRTM simulations for comparisons to VIIRS observations.

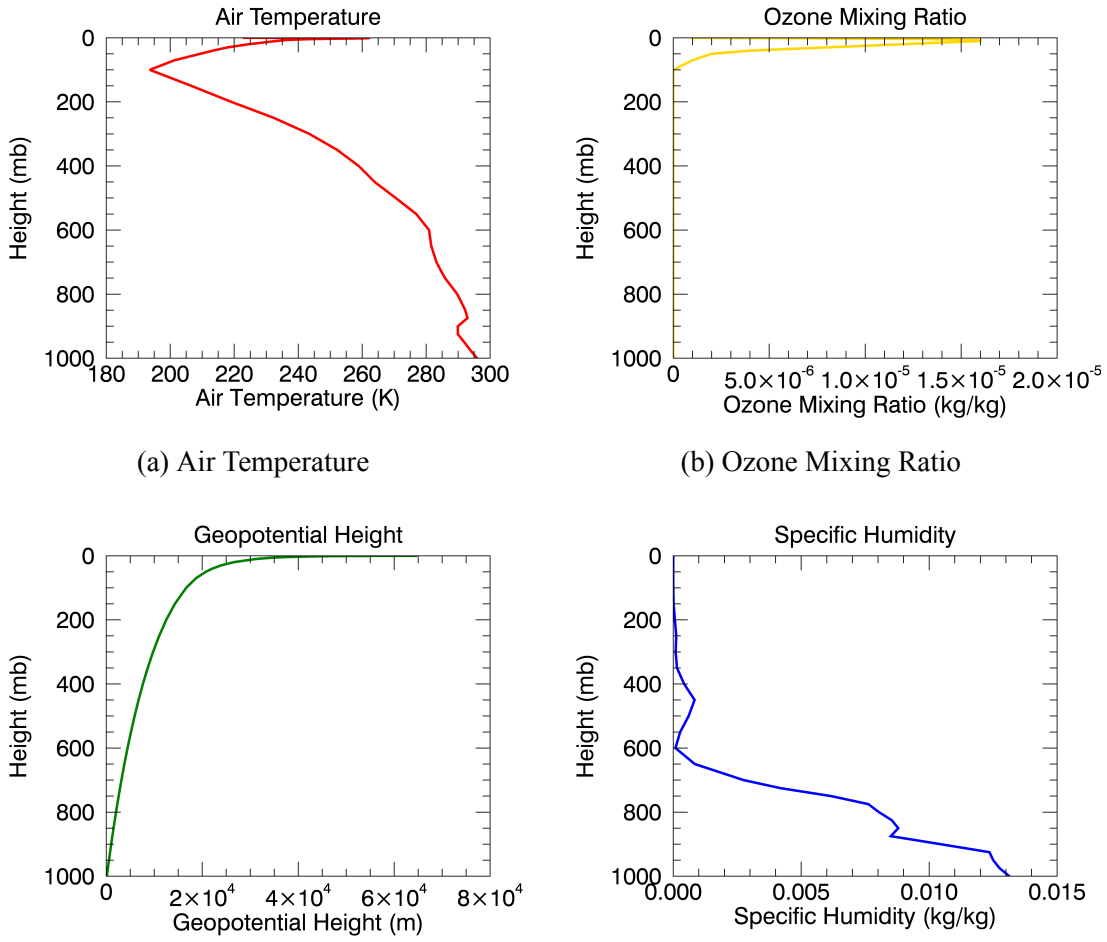

(a) Air Temperature

(b) Ozone Mixing Ratio

(c) Geopotential Height

(d) Specific Humidity

Figure 2.2: MERRA data 00 UTC

3 METHODS

The validation of the VFRTM involves a two-pronged approach of comparisons. The first is a comparison between simulators and the second is a comparison between simulated and observed results. Figure 3.1 shows the process of validation of the VFRTM from the data used through comparison of results. This serves as a good reference for the methods discussed at length in this section.

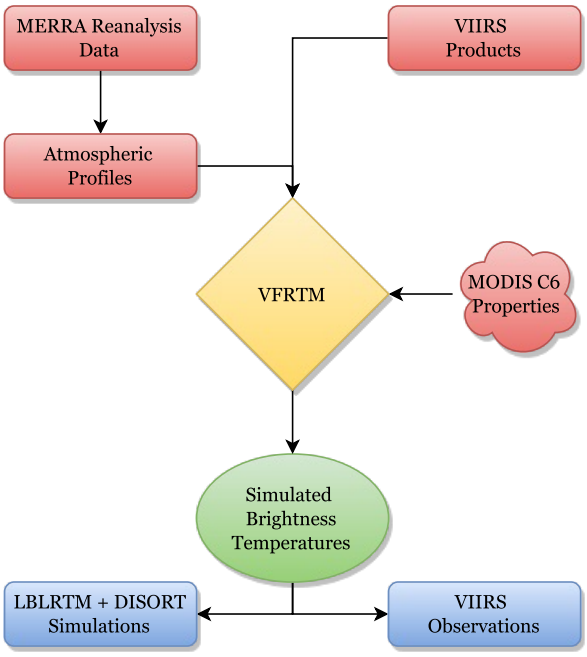

Figure 3.1: Flowchart outlining the process of validation for the VFRTM

3.1 LBLRTM + DISORT vs. VFRTM

By comparing the simulation output of LBLRTM + DISORT to those of VFRTM, the speed and accuracy of VFRTM can be validated. This method has been updated with

respect to previous studies by using MERRA profiles rather than idealized profiles for gaseous absorption and transmittance calculations. For use on a global scale, this provides the closest equivalent to real world data, and allows for improvement upon global scale retrievals.

3.1.1 LBLRTM + DISORT

The LBLRTM + DISORT assumes a plane-parallel, inhomogeneous atmosphere split into 80 discrete homogeneous and isothermal layers (an arbitrary choice), with more layers resulting in a more precise final result. The layers are written with a top down approach where level 1 is 50 km above the surface and level 81 is the surface of the Earth. From level 1 to 21 the atmospheric layers are 1 km deep, shrinking to 0.5 km in depth approaching the surface, with a cloud placed at level 61, 10 km above the surface. The atmospheric depth is set to 50 km rather than to 100 km (the border between the atmosphere and outer space) because the clouds in question should be well under the stratosphere and gases are treated as mixed in the layers above and below the cloud, thus the full depth of the atmosphere is not necessary for calculations. A TAPE5 file (atmospheric profile created using MERRA data) for each grid point is used as input into the LBLRTM, and a directory of 80 τ files is produced. The 80 τ files are combined into one transmission file, with those results being fed into DISORT.

Cloud information from MODIS Collection 6 (C6) is included into DISORT at this point. A MODIS collection is the processing or reprocessing of satellite obtained data using consistent algorithms (Platnick and Xio, 2014). Level-2 data such as τ, D_{eff}, and

water path for ice cloud thermodynamic phases were updated in MODIS C6 beginning in December 2013, with the most important update being the inclusion of the single habit severely roughened aggregate columns for ice clouds (Platnick and Xio, 2014). MODIS C6 data also included an analytical gamma distribution for the ice cloud model and smaller τ to remove the high bias of ice cloud τ in the IR from MODIS C5 (Holz et al., 2015; Platnick et al., 2015). The geometric and scattering properties of the MODIS C6 ice cloud model plotted for a visible wavelength of 0.65 μm as an example can be viewed in Figure 3.2. From Figure 3.2b it is discernible that the severely roughened surface from the aggre-

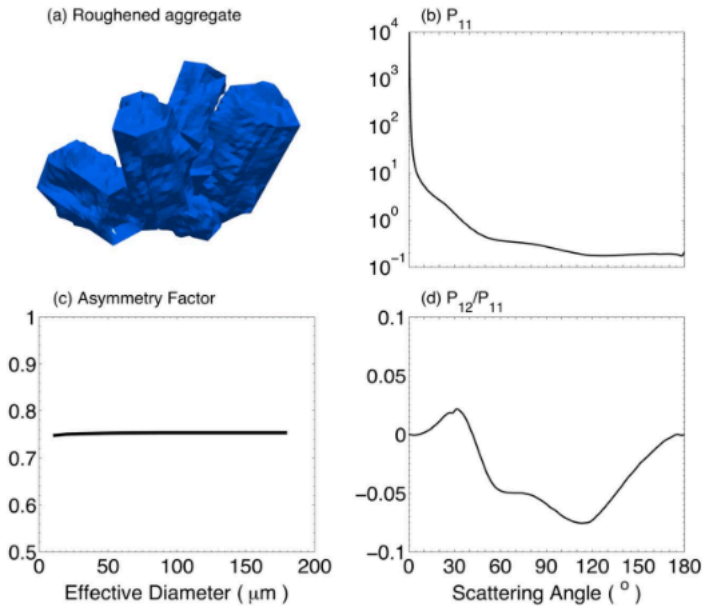

Figure 3.2: MODIS C6 ice cloud model: (a) geometry of an eight-column hexagonal aggregate with roughened surfaces, (b) phase function (P_{11}) of the aggregate with an effective diameter of 50 μm, (c) asymmetry factor as a function of D_{eff}, and (d) P_{12}/P_{11} element of the aggregates with a D_{eff} of 50 μm (Liu et al., 2014)

gate creates a very smooth phase function, decreasing the amount of back and side scatter by the particle. The consistency throughout D_{eff} sizes in Figure 3.2c demonstrates that

the asymmetry factor is independent of D_{eff} and represents primarily forward scattering (Wendisch and Yang, 2012). Similar results are expected in the IR, as scattering is reduced at IR wavelengths.

DISORT intakes the transmittance files calculated for each grid point and runs over each line of the spectrum before outputting the wave-number, D_{eff} and τ values, and spectral BT for each point over a specified satellite viewing zenith angle ranging from 0° to 80°. It is to be expected that the largest angle (80°) would represent the longest path length, the smallest amount of incident radiance, and the least accurate TOA BT at that location. Additionally, the smallest angle (0°) should represent the smallest path length, the largest amount of incident radiance, and therefore the most accurate TOA BT at that location. The primary conclusion taken from this is that BT accuracy and value should increase with decreasing angle, meaning the closer to zenith the satellite collects BT data, the more accurate and higher in value those returns will be compared to the same spot at a larger zenith angle. Closer to the horizon, there is higher potential for error to be introduced via pixel growth or increased path length. The selection of zenith angle used in calculations will depend on the test being run.

The BT values produced by LBLRTM + DISORT are presented in the form of spectral BT which need to be translated to band averaged BT in a series of three steps. First, spectral BT data is converted to spectral radiance values using the Planck's equation,

$$L(\nu,t) = \frac{c_1 \nu^3}{e^{c_2 \nu / t} - 1} \tag{3.1}$$

where $L(\nu,t)$ is blackbody radiance $[mW/m^2 - sr - cm^{-1}]$, $c_1 = 1.191042 * 10^{-5}$

$[mW/m^2-sr-cm^{-4}]$, $c_2 = 1.4387752\ [Kcm]$, ν is wavenumber $[cm^{-1}]$, and t is blackbody temperature $[K]$. The spectral radiances are then translated to band averaged radiances via integration over the weighted response functions interpolated over the spectrum, of each VIIRS channel. The integration is given by,

$$R = \frac{\sum \int R(\nu) SRF(\nu) d\nu}{\sum \int SRF(\nu) d\nu} \tag{3.2}$$

where R is the band averaged radiance, $R(\nu)$ is radiance, and $SRF(\nu)$ is the spectral response function. Finally, to convert band averaged radiance to band averaged BT, the inverse of the Planck's law is used.

$$t(\nu, L) = \frac{c_2 \nu}{ln(c_1 \nu^3 / L + 1)} \tag{3.3}$$

3.1.2 VFRTM

The IR simulator for the VFRTM has programs that work very similarly to those in LBLRTM + DISORT to allow for the final products to be compared. Modules that contain pre-calculated LUTs for gas absorption are used by CKD programs which intake atmospheric profiles (created using MERRA data), and calculate gaseous absorption and transmittance. These transmissivities are then used by the RTE solvers to simulate BT values. The CKD method is used for inhomogeneous paths and is an approximation of the k-distribution method used for a homogeneous path. CKD is given by,

$$\tau(u) = \int_0^1 exp[-\int_0^u k(g, u') du'] dg \tag{3.4}$$

where τ is optical depth, u is the location in the integration path, k is the absorption spectrum, and g is a representation of the interval of the absorption spectrum. The CKD method

takes only seconds to run one pixel and uses three orders of magnitude less computational effort than the LBLRTM + DISORT method which takes tens of minutes to run for just one pixel (Petty, 2006). This method avoids the use of brute force line-by-line method of calculating transmittances by using integrations computed over a smoother function via large discrete steps (used to reduce computational effort) that can allow for maintained accuracy. The CKD method allows for calculations to have overall errors of $< 1\%$ (Petty, 2006). The final result contains COP and BT values for all three channels that are already band averaged so no additional calculations or conversions need to be made.

3.1.3 Calculations and Inputs

When comparing two RTM simulations, there are several methods used to measure the accuracy of the VFRTM in relation to the benchmark results from LBLRTM + DISORT. The first is to compare BT simulations from both RTMs by plotting them in scatter plot form. Both models are run for clear sky and cloudy sky cases over four zenith angles: 0°, 20°, 40°, and 60°. For the clear sky case τ = 0.001 and D_{eff} = 0.001 μm. Extinction of radiation by scattering is negligible not only for particles of that size, but also in the IR region in general. In the absence of clouds, it is largely the absorption by gases that controls the opacity of the atmosphere, and with a τ value that small, nearly all radiation is transmitted to the surface (Petty, 2006). For the cloudy sky, three cases are considered: thin, medium, and thick. For the thin cloud τ = 0.1 and D_{eff} = 20 μm, for the medium cloud τ = 3 and D_{eff} = 50 μm, and for the thick cloud τ = 8 and D_{eff} = 100 μm. A cloud is considered optically thin if $\tau << 1$ and optically thick if $\tau >> 1$. The object of this

test is to show strong correlation of BT values for a given pixel between simulations of the slow and fast models, with a low level of error to show the accuracy of the fast model.

A second analysis that can be done is to look at the BTD between the two simulations. For this test 10 points were picked at random from each granule, and the simulator was run at a zenith angle of 20° for various COP. A zenith angle of 20° has been used in previous studies, and it represents an angle that sees more than what is directly under the satellite but also is not subject to large amounts of pixel growth. To be representative of an atmosphere with ice clouds, D_{eff} was set to 20, 50, 80, 110 μm and was run over τ values of 0.01, 0.03, 0.05, 0.1, 0.3, 0.5, 1, 1.5, 2, 2.5, 3, 4, 5, 6, 7, 8, 9, 10, 20, and 30. Using a range of τ from optically thin through optically thick will help to show any sensitivities to or dependencies on τ for VFRTM. The lower the differences, the more accurate the fast model is. While all of the same input values are used for both LBLRTM + DISORT and VFRTM, a specific input text file is used for the VFRTM simulation. An example of the input file can be found in Table 3.1.

3.2 VFRTM vs. VIIRS Observations

Comparing BT values simulated by VFRTM to those observed by VIIRS can provide validation of the use of MODIS C6 data. This method also allows for a higher-resolution comparison than that of the previous section. Surface temperature, satellite viewing zenith angle, τ, D_{eff}, and cloud top height (cloud layer) are adjusted for each pixel run through VFRTM. VIIRS data from June 21, 2014 is used as a case study. This is an improve-

Table 3.1: Example of Data in 'input.txt' File for BTD Plot Simulations

1	Number of cloud / aerosol layers
1	Cloud_type (0: water, 1:ice) from bottom to top
61	Cloud_layer (1: at TOA size_layer: boundary cloud)
20	Number of cloud layer loops
0.01	Optical Depth (Additional values included depending on the test)
20.	Effective Size (Additional values included depending on test)
299.0	Surface Temperature
0	Albedo Type (0: constant 1: user_defined)
0.02	Surface albedo if albedo type = 0 (1-emissivity)
20.0	Viewing zenith angle (degree)
1	Code of satellite instrument (1: VIIRS, 2: MODIS)

ment upon previous studies that used RMS error to select appropriate COP values or used MODIS COP to compare directly to VIIRS simulations. This study uses VIIRS data products to simulate BT for the granule to compare to the actual observed BT in an attempt to demonstrate performance accuracy.

3.2.1 VIIRS

To make comparisons to VFRTM, latitude, longitude, satellite viewing zenith angle, τ, D_{eff}, and BTs are taken from VIIRS_SDR data sets, and COP and cloud top heights were collected from VIIRS_IPNG data sets. The data for surface temperature is taken from MERRA 1,000 mb air temperatures averaged between 09 UTC and 12 UTC to give the approximate surface temperatures at 10:30 UTC. This is the closest time to that of the VIIRS data in use, 10:38-10:44 UTC.

The BT values are stored as 16-bit unsigned integer arrays and as such must be converted to proper scientific units using scale and offset values provided in a two-element

vector of 32-bit floating point values where the first value represents the 'scale value' and the second value represents the 'offset value' (Seaman et al., 2014). Using

$$f = c_0 n + c_1 \tag{3.5}$$

where c_0 is the scale value, c_1 is the offset value, and n represents the unsigned integer value, and the values in Table 3.2, the BT values can be converted.

Table 3.2: Scaling Values for VIIRS BT Values

Channel	**Scale Value**	**Offset Value**
M14	c_0 = 0.00373892	c_1 = 120.000
M15	c_0 = 0.00412044	c_1 = 111.000
M16	c_0 = 0.00425779	c_1 = 103.000

An additional issue is the use of fill values from bow-tie removal within the data sets. Those found within VIIRS data are listed in Table 3.3 along with their meanings (Seaman, 2013). Surface temperature data from MERRA also contains NaN values in

Table 3.3: Fill Values for VIIRS Data

Array Value	**Name**	**Meaning**
65533	OBPT	On-board pixel trim
-999.5	ERR	Error during processing or non convergence
-999.6	OGPT	On-ground pixel trim
-999.9	N/A	Not applicable value

similar locations to the VIIRS bow-tie removal spots. These values must also be removed, and if they are not, they could lead to erroneous simulations that could skew results and analysis. Once the fill values are removed, the input can be used in the VFRTM to simulate

the BT values that VIIRS observed. Plots of the observed and simulated BT values are created for analysis.

4 RESULTS

4.1 Simulation vs. Simulation

Comparing the results of the benchmark value simulations of LBLRTM + DISORT to those of VFRTM allows for an analysis of the accuracy of the VFRTM. The VFRTM can be validated if the errors are small. Several criteria are used to assess the accuracy of the VFRTM.

4.1.1 Scatter Plot Analysis

The first method is use scatter plots of VFRTM versus LBLRTM + DISORT. This provides a visual representation of the correlation between the two models. As a reference, a 1-to-1 line is plotted for each case. The amount of linear correlation is given by the correlation coefficient,

$$r = \frac{\sum(x-\bar{x})(y-\bar{y})}{\sqrt{\sum(x-\bar{x})^2(y-\bar{y})^2}} \tag{4.1}$$

where x represents the LBLRTM + DISORT values, y represents the VFRTM values, and $\bar{x}$ and $\bar{y}$ represent the sample means of those arrays. The RMS difference of the BTs provides a measure of the magnitude of the difference between the two models given by

$$RMS(BTD) = \sqrt{\frac{\sum_i^N (BTD_i)^2}{N}} \tag{4.2}$$

where BTD_i at the i^{th} point is represented by,

$$BTD = BT_{VFRTM} - BT_{LBLRTM+DISORT} \tag{4.3}$$

and N is the total number of points. Percent error is also used to represent relative error of the model given by,

$$Relative\ Error = \frac{|Measured\ Value - Actual\ Value|}{Actual\ Value} \tag{4.4}$$

Using the data from both June 20, 2014 (day case) and June 21, 2014 (night case), clear sky and cloudy sky tests are run.

First, for the clear sky case BT was simulated for both LBLRTM + DISORT and VFRTM for June 21, 2014 over four zenith angles (0°, 20°, 40°, and 60°) with τ = 0.001 and D_{eff} = 0.001 μm. Each test was run over a 1° by 1° grid (ultimately containing 540 points) within the granule for each of the three longwave channels. Figure 4.1 gives an example of these plots for channels M14, M15, and M16 at a zenith angle of 20°. The results of tests using zenith angles 0°, 40°, and 60° can be found in Appendix A. The statistical analysis for the clear sky case calculations at all four tested zenith angles found in Table 4.1. Correlations for all cases range between r = 0.92 and r = 0.96 with RMS error between 0.3 K and 0.7 K, increasing for increasing wavelength and zenith angle. This level of RMS error corresponds to $<$ 0.25% of error from the VFRTM, and the low level of percent error shows that the VFRTM would be accurate to use for clear sky cases. The discrepancy between simulated BT may be due to the way that variable is processed with such small COPs. In general, the points further from the 1-to-1 line in the clear sky case have higher BT values simulated by VFRTM. This is not the case for the cloudy sky tests.

Continuing to use data from June 21, 2014, simulations were run for "thin" (τ = 0.1, D_{eff} = 20 μm), "medium" (τ = 3, D_{eff} = 50 μm), and "thick" (τ = 8, D_{eff} = 100

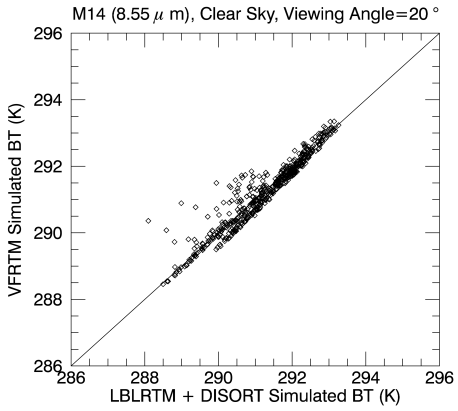

(a)

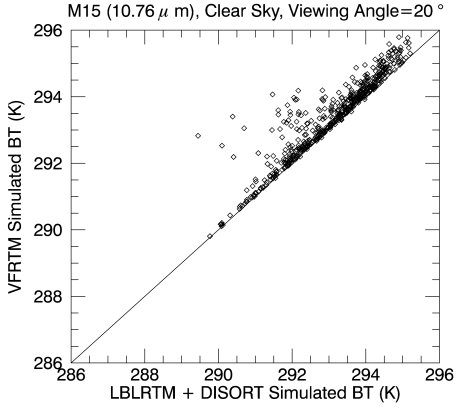

(b)

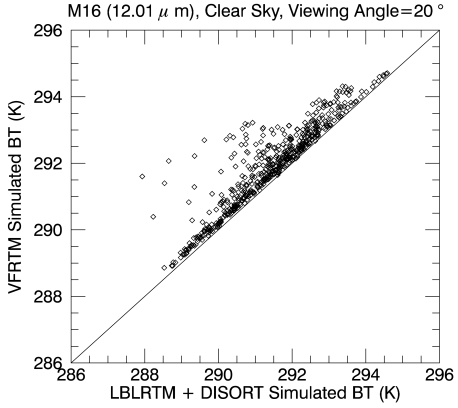

(c)

Figure 4.1: Clear sky example channels M14 (a), M15 (b), and M16 (c)

Table 4.1: Clear Sky Example: Statistical Analysis

Angle	M14		M15		M16	
	r	***RMS Error***	***r***	***RMS Error***	***r***	***RMS Error***
0°	0.96	0.30 K	0.94	0.52 K	0.92	0.70 K
20°	0.96	0.31 K	0.94	0.54 K	0.92	0.72 K
40°	0.94	0.36 K	0.92	0.60 K	0.92	0.76 K
60°	0.94	0.42 K	0.93	0.74 K	0.96	0.74 K

μm) clouds. Again, each case has 540 points from the 1° by 1° grid plotted for each channel. Plots for the 20° zenith angle cases are shown in Figure A.5 along with statistical analysis for all zenith angles tested in Table 4.2. Plots for the other zenith angles tested can also be found in Appendix A. Overall the correlation for all cases is extremely high with r $>$ 0.99. This result is further backed up by the RMS error ranging from 0.137 for thin clouds to 0.166 for thick clouds. The corresponding error is $<$ 0.06% for all cases, which is approximately a quarter of the error from the clear sky case. Error is essentially constant in each cloud case between increasing wavelength and increasing zenith angle showing very little sensitivity to either variable. Error does increase with cloud thickness, but for each of the three cases presented and all cases in between, the VFRTM is extremely accurate when compared to the benchmark simulations produced by LBLRTM + DISORT.

Comparing the clear sky case to the cloudy sky cases, the cloudy sky cases are much more accurate than the clear sky cases. Although the same data are used to create atmospheric profiles for gaseous absorption and transmittance calculations for both the clear sky and cloudy sky cases, the VFRTM shows better accuracy in the cloudy sky calculations. The slightly lower accuracy in the clear sky case may be due to the COP used. It may be

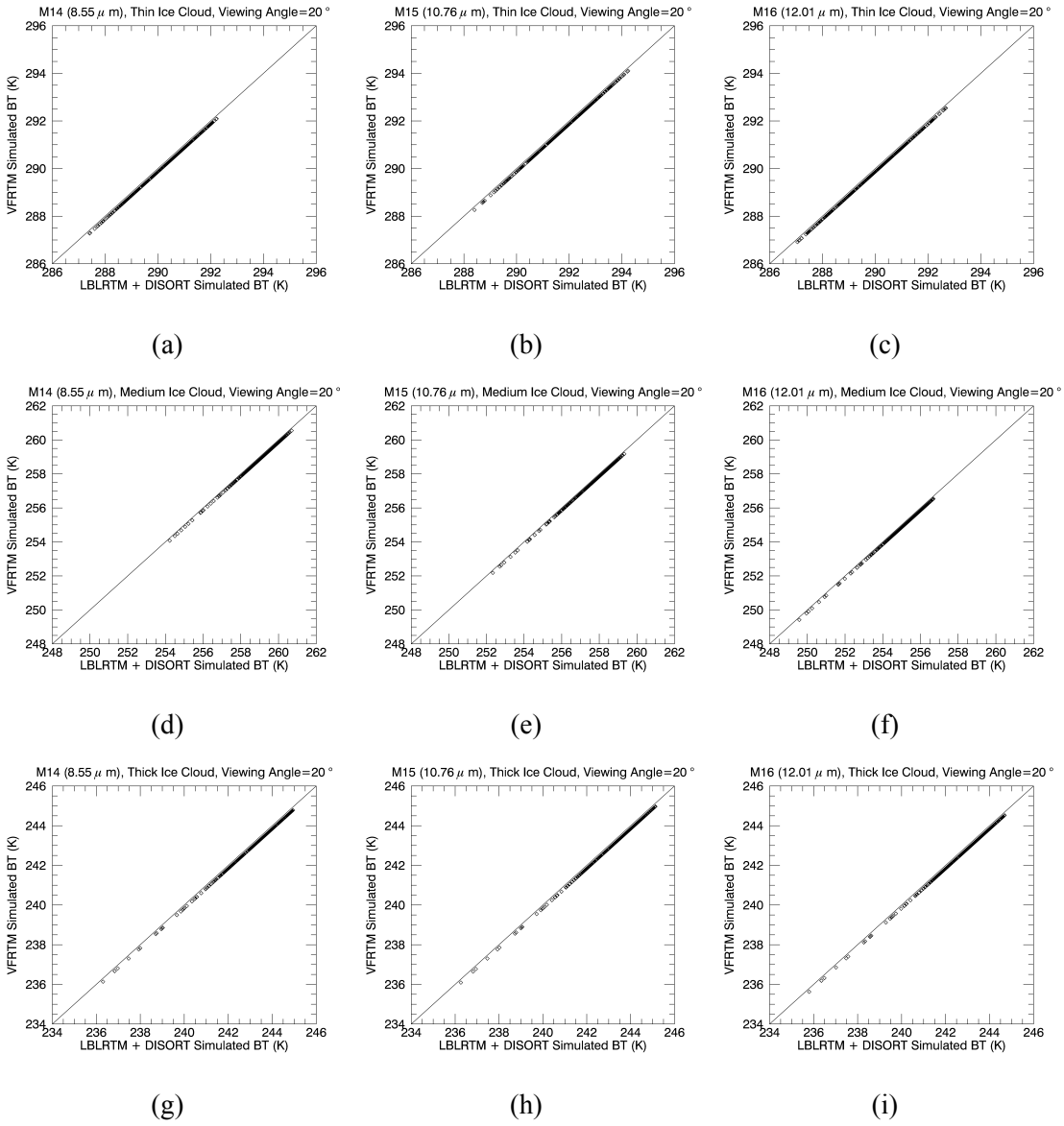

Figure 4.2: Cloudy sky examples channels M14, M15, and M16: (a)-(c) thin, (d)-(f) medium, (g)-(i) thick

Table 4.2: Cloudy Sky Examples: Statistical Analysis

Thin Cloud						
Angle	**M14**		**M15**		**M16**	
	r	***RMS Error***	***r***	***RMS Error***	***r***	***RMS Error***
0°	0.99	0.14 K	0.99	0.14 K	0.99	0.14 K
20°	0.99	0.14 K	0.99	0.14 K	0.99	0.14 K
40°	0.99	0.14 K	0.99	0.14 K	0.99	0.14 K
60°	0.99	0.14 K	0.99	0.14 K	0.99	0.14 K
Medium Cloud						
Angle	**M14**		**M15**		**M16**	
	r	***RMS Error***	***r***	***RMS Error***	***r***	***RMS Error***
0°	0.99	0.15 K	0.99	0.15 K	0.99	0.16 K
20°	0.99	0.15 K	0.99	0.16 K	0.99	0.16 K
40°	0.99	0.16 K	0.99	0.16 K	0.99	0.16 K
60°	0.99	0.16 K	0.99	0.16 K	0.99	0.16 K
Thick Cloud						
Angle	**M14**		**M15**		**M16**	
	r	***RMS Error***	***r***	***RMS Error***	***r***	***RMS Error***
0°	0.99	0.16 K	0.99	0.16 K	0.99	0.16 K
20°	0.99	0.16 K	0.99	0.16 K	0.99	0.16 K
40°	0.99	0.17 K	0.99	0.17 K	0.99	0.17 K
60°	0.99	0.17 K	0.99	0.17 K	0.99	0.17 K

that the VFRTM is just not as accurate for a clear sky case as for a cloudy sky case because of the way it handles such small COPs, and the model may just perform the best when there are clouds involved in the simulation. Multiple scattering is still accounted for in the VFRTM for clear sky cases (unlike in previous studies) and as such may be contributing to the error level. Further research should be done on clear sky simulations to determine if the amount of error can be reduced further to the level of the cloudy sky simulations.

In an attempt to determine any differences between day and night simulations, a set of cloudy sky tests were done for the daytime granule from June 20, 2014. Due to the

accuracy level of the clear sky case as well as the accuracy level of the various zenith angle tests that were run for the nighttime granule, only the cloudy sky cases were tested at a zenith angle of 20° for this data set. Plots for the three cases can be found in Appendix A (as they look similar to those from June 21, 2014), while the statistical analysis results can be found in Table 4.3. There are several erroneous points in each plot that lead to a minimal reduction in correlation in comparison to the nighttime case. RMS error for these cases is much more variable (possibly due to the erroneous points), but has around half the amount of error as the nighttime cases except for a few channels. The values of RMS error represent error from the VFRTM as low as 0.01% in some cases.

Table 4.3: Cloudy Sky Examples (June 20, 2014): Statistical Analysis

Angle	**M14**		**M15**		**M16**	
	r	***RMS Error***	***r***	***RMS Error***	***r***	***RMS Error***
Thin	0.99	0.17 K	0.99	0.08 K	0.99	0.22 K
Medium	0.99	0.11 K	0.99	0.05 K	0.99	0.04 K
Thick	0.99	0.08 K	0.99	0.09 K	0.99	0.03 K

When comparing the daytime cases to the nighttime cases, RMS error is much lower during the day and corresponds to a lower amount of error in the VFRTM simulations. Overall, the thicker clouds are handled better by the model during the day, and the thin cloud is handled better by the model at night. BT values between day and night cases are also different, as is expected. As mentioned previously, high cirrus clouds act as blackbodies, with thin cirrus clouds being an exception. High, thin clouds have similar BT values during the day and night. These clouds are so thin that they cause a reaction similar to the

clear sky case. During the day solar radiation transmits through the clouds to the surface. Because the cloud is so optically thin, the imager sees a BT similar to the surface temperature rather than the temperature at the top of the cloud. At night the process is similar, with terrestrial radiation emitted from the surface and passing through the cloud (rather than being absorbed) so that the imager also sees a value similar to that of the surface. As the clouds become thicker, they act more like blackbodies, and the values recorded by the imager are more representative of their altitude.

During the day, for high, thick clouds, solar radiation still passes through the cloud to the surface where it is absorbed into the surface of the Earth. A small amount of solar radiation is reflected off the top of the cloud towards the imager immediately. The BT values are representative of the cloud top with the thickest clouds having the coldest values due to lack of interaction of terrestrial radiation that is seen in the medium cloud case. At night, the reasoning is similar, but the terrestrial radiation is emitted with a value of the surface temperature causing the BT values of the clouds to be higher at night than during the day. High clouds trap terrestrial emission through absorption with radiance being re-emitted towards the Earth's surface or lost out to space where it is detected by VIIRS. Again, the thicker clouds have lower BTs as they trap more of the surface radiance than the medium clouds. Knowing the BT values expected from various cloud types during the day and the night could improve global cloud retrievals. The COP of each cloud type tested is important to know to make broad-based assumptions from simulations on a global scale. BTD and RMS error are used to test the sensitivity of simulations to COP in an attempt to

improve the methods of operational uses of radiative transfer techniques.

4.1.2 Brightness Temperature Difference Analysis

The second method used in this study to validate the accuracy of the VFRTM is to calculate BTD for a select few points from each date using Equation 4.3. These plots are a function of τ and D_{eff} and help to test the sensitivity of the VFRTM to these COP in the IR region of the electromagnetic spectrum. A BTD = 0 would show that the simulation from VFRTM is equal to that of the LBLRTM + DISORT while a BTD $>$ 0 represents VFRTM simulations being greater than those from LBLRTM + DISORT and BTD $<$ 0 represents VFRTM simulations being less than those from LBLRTM + DISORT. The smaller the magnitude of the differences calculated, the more accurate the VFRTM is. Statistical analysis is done in the form of RMS error of BTD calculations. For each data granule, 10 randomly selected pixels were plotted and analyzed. BTD is calculated for four D_{eff} values over a series of τ values representative of what may be seen in an atmosphere with an ice cloud. The RMS error calculations were done with the data from those 10 points and based on the consistency in results from those points, the magnitude of error is representative of the full data granule.

For both data granules, one set of BTD plots will be analyzed here with others available for viewing in Appendix B. First looking at 18°N/124°W from June 20, 2014, Figure 4.3 shows several discernible features that are also prevalent in the other pixels tested. In Figure 4.3a there is a large dip around τ = 5 that is only present for the M15 band and not present in the figures with larger D_{eff} sizes. Another primary feature found in all of

the plots is the "spike" in BTD found at τ = 1.5 for all channels regardless of D_{eff} size. This spike is an increase in the magnitude of BTD and represents a less accurate result of the VFRTM at that thickness. This could be an issue with how this τ interacts with the data profiles, or there could be an issue with the simulation for a particle of this size. For this pixel, all values are < 0 showing that the simulated VFRTM results for this pixel are smaller than those produced by LBLRTM + DISORT. In general, for the June 20, 2014 cases, BTD $<$ 0.3 K with BTD decreasing to $<$ 0.15 K for increasing D_{eff} values. For increasing τ, BTD values for each channel decrease to a constant value that is different for each channel, but which is between 0 and magnitude 0.1 for all cases. This shows that past the point of approximately τ = 10, the VFRTM has no sensitivity to τ, given that optically thick clouds act as blackbodies.

For June 21, 2014, a very similar result is found. The large dip in 4.4a for channel M15 around τ = 5 is still visible and all subplots in Figure 4.4 contain the same spike at τ = 1.5 for all channels. The results for this data set are the same order of magnitude as the previous set with all pixels having a BTD $<$ 0.3 K with values reducing to $<$ 0.1 K with increasing τ. Similarly to the other data set, each channel has a constant value BTD value between 0 and 0.1 K. Due to the strong agreement in results between both data sets, the VFRTM is highly accurate when compared to the simulations of LBLRTM + DISORT.

Lastly, using RMS error calculations, the accuracy of the VFRTM can be further demonstrated by providing a meaningful measure of the error in the differences between the two simulations. These results are used as an index for the overall error level of the

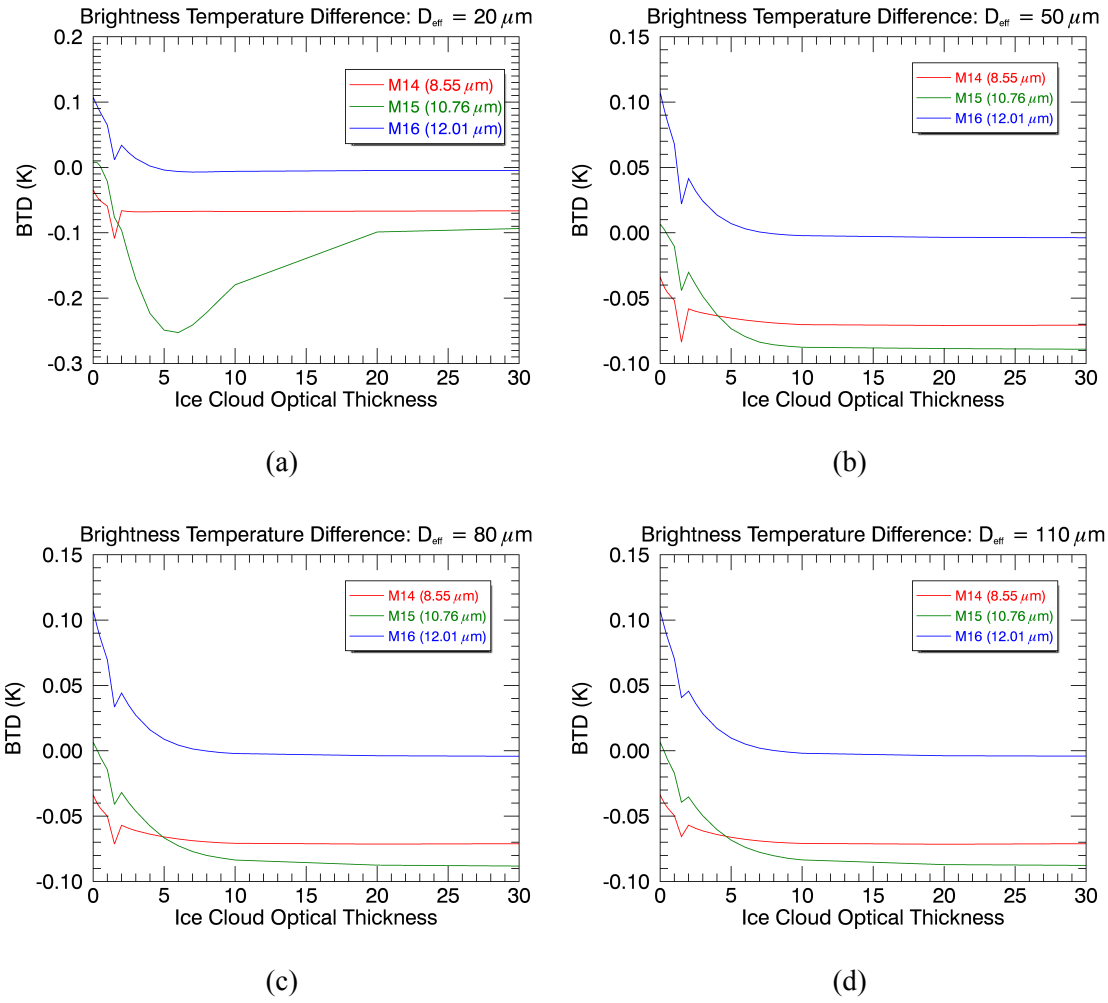

Figure 4.3: Brightness temperature difference for 18°N/124°W June 20, 2014

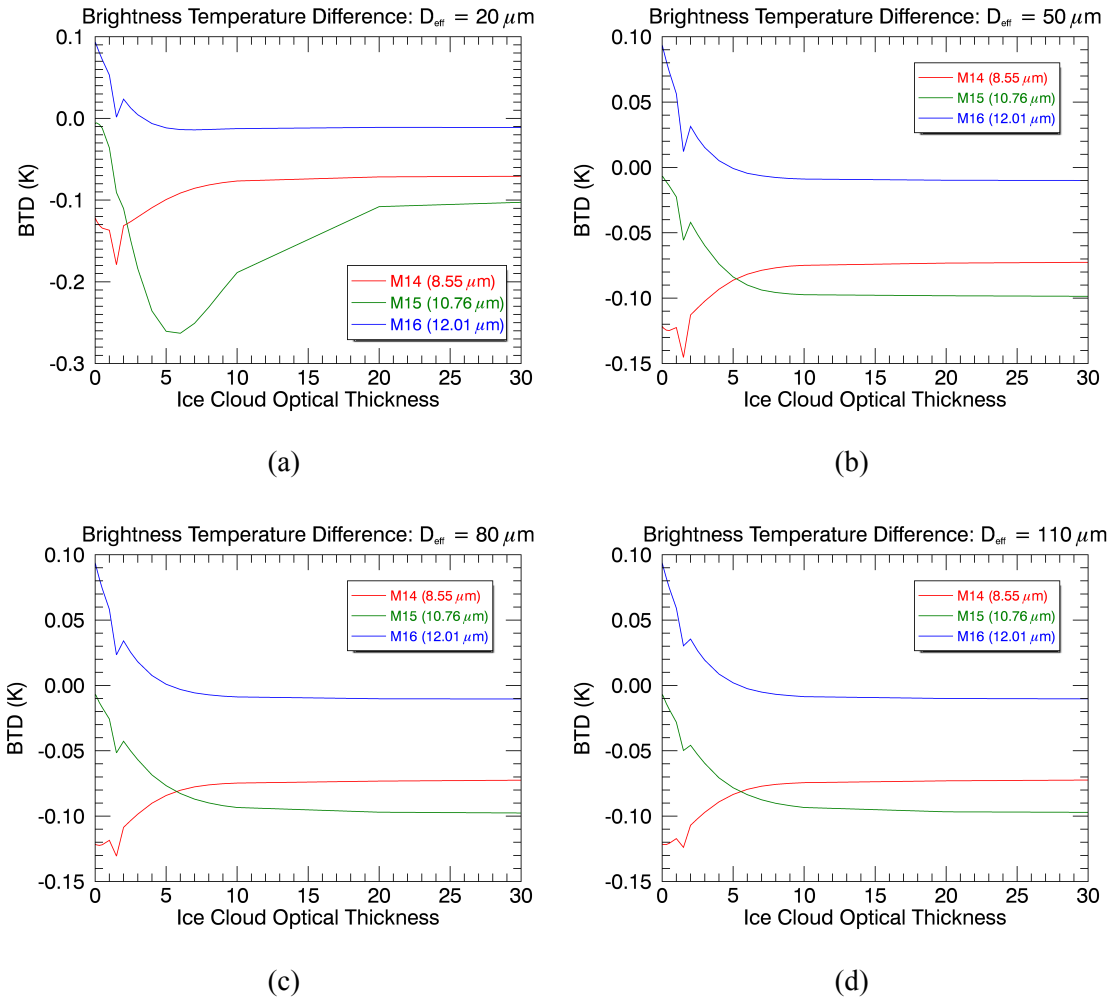

Figure 4.4: Brightness temperature difference for 23°N/137°W June 21, 2014

VFRTM. Based on the work done by Niu et al. (2007), Zhang et al. (2007), and Ding et al. (2011), an appropriate level of error for the VFRTM under ice cloud conditions in the long wave IR channels is on the order of 0.5 K. RMS error was calculated using data from each of the 10 random points plotted for each data set, for each IR channel, and an overall value for each D_{eff} size. Values for June 20, 2014 and June 21, 2014 can be found in Table 4.4.

Table 4.4: Root Mean Square Error Values

June 20,2014				
D_{eff}	**M14**	**M15**	**M16**	**All**
20 μm	0.12 K	0.15 K	0.07 K	0.12 K
50 μm	0.11 K	0.07 K	0.07 K	0.09 K
80 μm	0.11 K	0.07 K	0.07 K	0.095 K
110 μm	0.11 K	0.07 K	0.07 K	0.09 K
June 21,2014				
D_{eff}	**M14**	**M15**	**M16**	**All**
20 μm	0.19 K	0.15 K	0.08 K	0.15 K
50 μm	0.18 K	0.06 K	0.08 K	0.12 K
80 μm	0.18 K	0.06 K	0.08 K	0.12 K
110 μm	0.17 K	0.06 K	0.08 K	0.12 K

The results show that for both dates and all cases, the RMS is < 0.2 K which demonstrates that the VFRTM is highly accurate for the ice cloud case based on the appropriate level of error from previous studies. This result is much better than those found in previous studies which may be due to the use of MERRA reanalysis data rather than idealized profiles. Some previous studies have lower RMS error, but that may be due to the use of idealized profiles or treatment of gases. In general, the level of error is higher for smaller D_{eff} in both the day and the night cases. This shows that there is higher sensitivity of the models to smaller cloud particles. In terms of the tests run for each channel, for both data

sets, M14 has the highest error followed by M16, then M15. Each channel is more sensitive to a specific atmospheric absorber, but since they are combined in the VFRTM to save on computation time, there could be increased levels of error with certain IR channels.

As BTD plots are used to show the sensitivity to COP, RMS error values were calculated for four τ values of various orders of magnitude using data from all three IR channels. Between the day and the night case found in Table 4.5, error is very similar for large τ for all D_{eff}. This is not surprising as these thicker clouds are essentially acting as blackbodies and the influence of COP in simulations is negligible. Error levels begin to diverge at smaller τ with the daytime case having higher accuracy in simulations than the nighttime case. During the night when RMS error from the scatter plots showed that the model is more accurate with thin cloud calculations, there is also higher sensitivity to the COP than during the day. Overall, VFRTM has a higher sensitivity to smaller D_{eff} and τ pairs.

Table 4.5: Root Mean Square Error Values for Various τ

June 20,2014				
D_{eff}	τ **= 0.01**	τ **= 1.5**	τ **= 10**	τ **= 30**
20μm	0.12 K	0.12 K	0.11 K	0.07 K
50μm	0.12 K	0.10 K	0.07 K	0.07 K
80μm	0.12 K	0.09 K	0.07 K	0.07 K
110μm	0.12 K	0.09 K	0.07 K	0.07 K
June 21,2014				
D_{eff}	τ **= 0.01**	τ **= 1.5**	τ **= 10**	τ **= 30**
20μm	0.17 K	0.16 K	0.12 K	0.07 K
50μm	0.17 K	0.14 K	0.07 K	0.07 K
80μm	0.17 K	0.13 K	0.07 K	0.07 K
110μm	0.17 K	0.12 K	0.07 K	0.07 K

4.2 Simulation vs. Observation

To compare the results of the simulation to the VIIRS observations, data from June 21, 2014 are used as a case study. BTs are simulated using geolocation and COP information from VIIRS itself. Atmospheric profiles and surface temperatures are from MERRA and are averaged between 9 UTC and 12 UTC to provide data as close as possible to the time of the VIIRS data. Comparing the simulated BTs to those observed by the VIIRS sensor provides a validation of the use of MODIS C6 data, as well as a validation of the accuracy of the VFRTM at a higher-resolution. The observed BTs in Figure 4.5 look reasonable. The coldest values represent high cloud tops, where there may be thunderstorms or high cirrus clouds, and the warmest values represent lower cloud tops. Unfortunately, the simulations show little consistence with the observed values. After looking further at the D_{eff} data from the VIIRS COP data, there are many values of 0.5 μm. These data are likely erroneous and should have been treated as fill values. Furthermore, clouds under 4 km are water clouds and could skew the final results.

After removing the pixels with erroneous values of D_{eff} and low water clouds, a much better result is obtained. The structure of high cloud tops associated with convection is visible in both images (see Figure 4.6). The same cloud structures are visible in both the observed and simulated cases unlike the previous set of images where there is no consistency between images. After adding back in the De_{eff} values but leaving out the low ice clouds, the large amount of error remains. This shows that the primary issue is the inclusion of the D_{eff} = 0.5 μm values. There is good agreement between the simulated

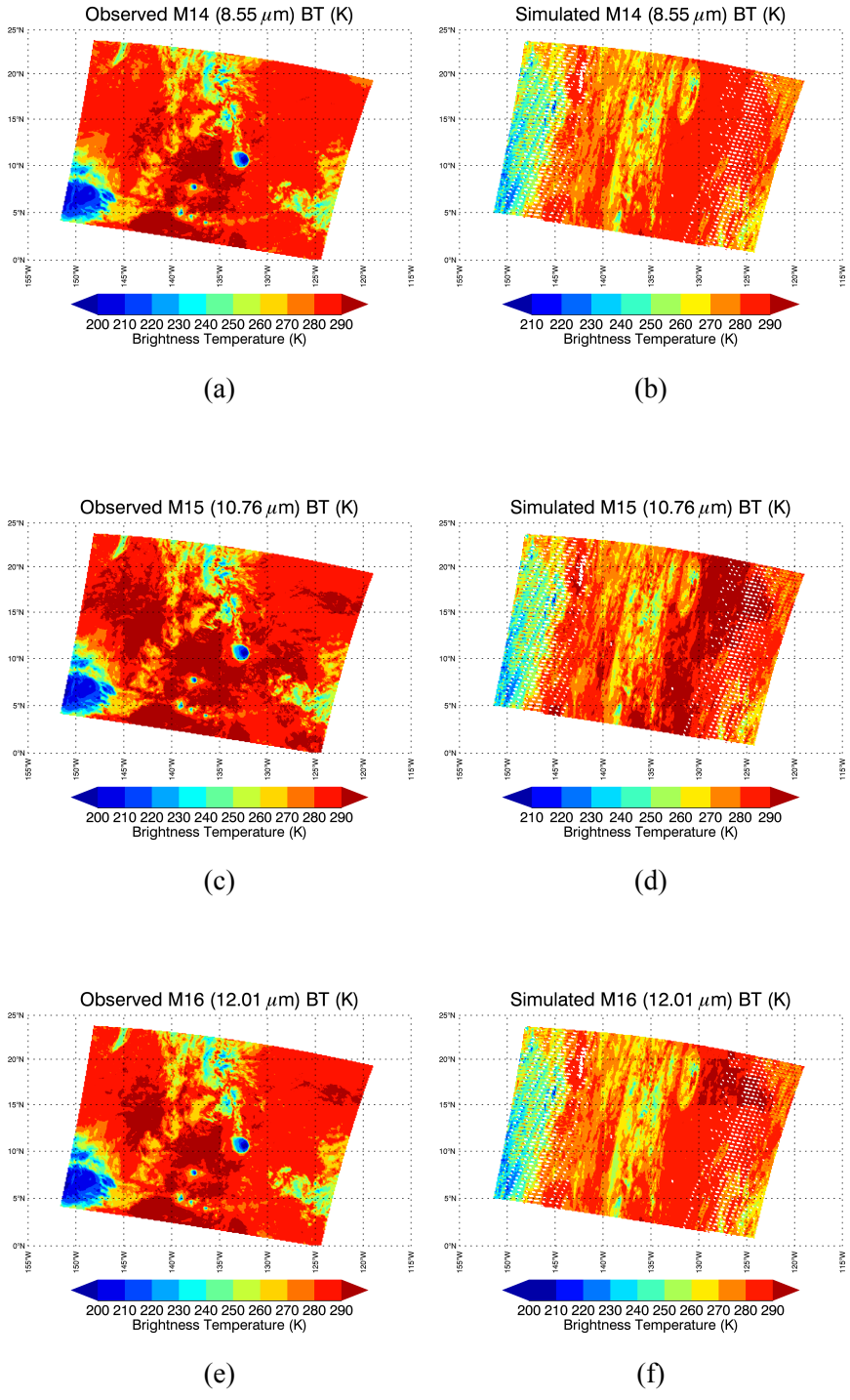

Figure 4.5: Initial comparison between observed (left column) and simulated (right column) brightness temperatures

and observed BTs. Table 4.6 shows the low level of RMS error as well as the percent error for each channel which represents the amount of error from the VFRTM in BT simulations for this case study. The RMS error increases for increasing wavelength. This may be due

Table 4.6: Case Study: Statistical Analysis

	M14	**M15**	**M16**
RMS Error	2.70 K	2.83 K	3.83 K
Percent Error	1.0%	1.1%	1.5%

to reduced scattering at longer wavelengths leading to an increase in difference between simulated and observed BT, which could mean VFRTM needs improvement on how scattering is handled. Similarly, the relative error also increases as wavelength increases, but the overall error amount is very low. The results of this statistical analysis show that not only is it possible to simulate BT at high resolutions on a large scale, but that the result is highly accurate. This could lead to strong improvements of global cloud retrieval and a better understanding of the effects of cirrus clouds on the global energy budget as well as an improvement to their contribution in global climate models.

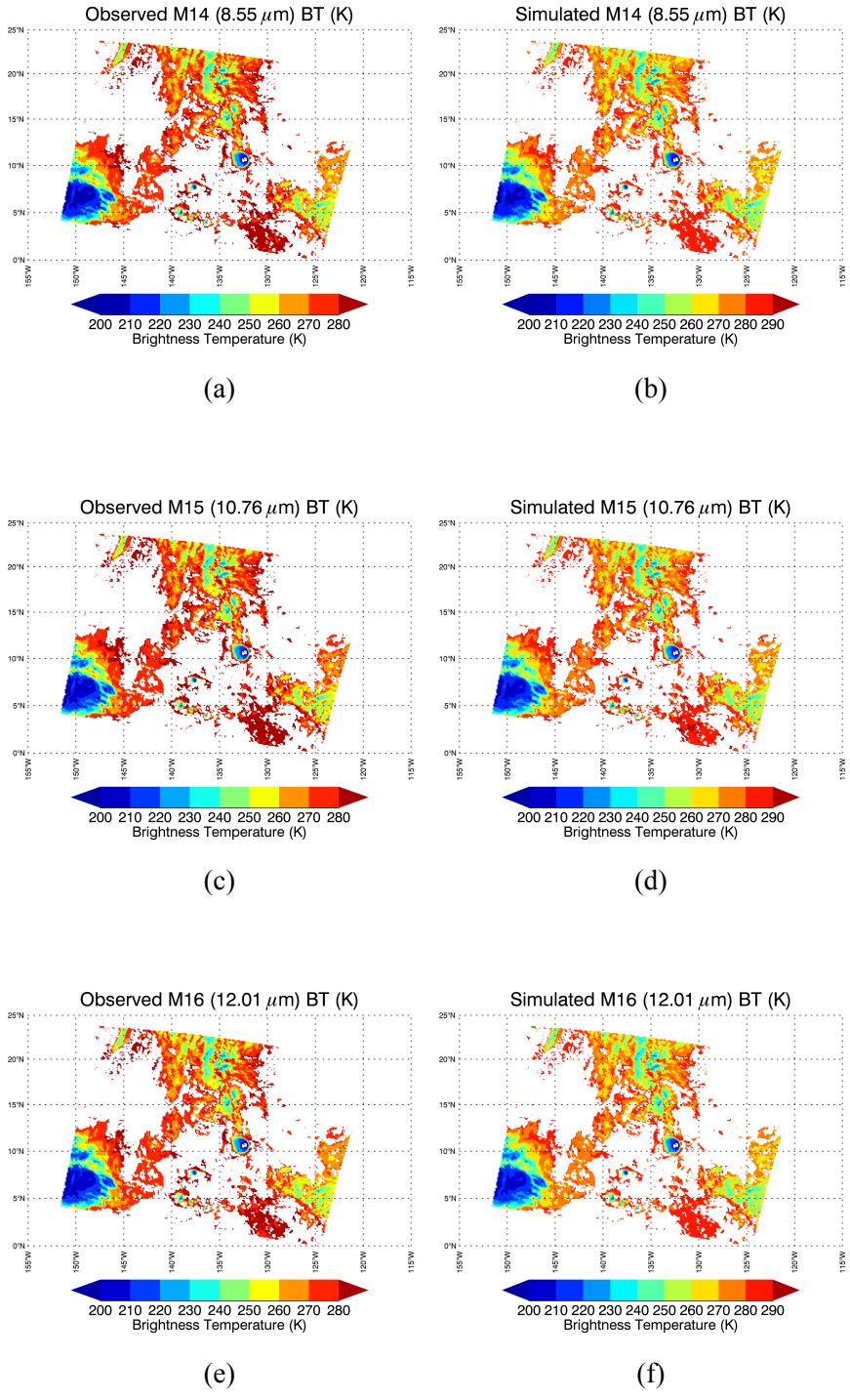

Figure 4.6: Comparison between observed (left column) and simulated (right column) brightness temperatures after removing fill values and water clouds

5 SUMMARY AND CONCLUSIONS

Clouds are an integral part of the balance of the global energy budget. Cirrus clouds are not represented well within the breakdown of the global energy budget because so much is still unknown about their spatial and temporal distribution, their COPs, and their contribution of warming from the positive climate feedback loop they create. Using a combination of remote sensing techniques and RTMs, BTs of clouds can be simulated, and COPs can be retrieved. With a better knowledge of the COPs of cirrus clouds and their amount of global coverage, the global energy budget and global climate models can be updated.

Before using an RTM for global retrieval purposes, the RTM needs to be validated. The well validated LBLRTM + DISORT is used to produce "benchmark" simulations to compare to those of the VFRTM. BT values are the best method of simulation for clouds in the IR spectrum because they provide the best measure of radiance with scattering reduced in that portion of the electromagnetic spectrum. Comparing the simulations of the VFRTM to those of the LBLRTM + DISORT provides a measure of accuracy for the VFRTM. Data from MERRA, VIIRS, and MODIS C6 are used as input data for BT simulations.

Accuracy is documented through several types of comparisons. First a comparison of BTs are presented in terms of scatter plots. Clear sky and cloudy sky cases are tested for various COP pairs for both a daytime and nighttime case. Error is higher for the clear sky cases than the cloudy sky cases. This should be investigated further. The level of error

could be due to how the VFRTM handles the lack of cloud particles. For the cloudy sky cases, error was much lower with error increasing slightly for increased τ. Comparing the results of the cloudy sky cases of the daytime case and the nighttime case, there is lower error overall for the daytime cases. Thicker clouds are handled better by the model during the day, and thinner clouds are handled better by the model during the night. Further case studies should be conducted to confirm this possible diurnal effect.

BTD analysis is also done for a select few pixels from both the daytime case and the nighttime case. These plots are used as a test of sensitivity of the model to various COP values. A spike in values occurs at $\tau = 1.5$ in all cases. This τ value does not interact well with the data profiles or is just not handled well by the simulator. Upon removing those data, a smoother result is obtained. In general, error decreases for increasing τ and is never more than 0.3 K for smaller COP. In terms of RMS error, an appropriate level of error is considered to be < 0.5 K based on previous studies. For all channels and all D_{eff}, error is < 0.2 K. This shows a high level of accuracy for the VFRTM when reanalysis data is used. Again the error was lower during the day, but for both cases, the highest sensitivity of the model was for the smallest COP pair.

A final test for accuracy is done by comparing the observations of VIIRS to the simulations of VFRTM. This provides a test of accuracy at a much higher resolution than previous tests and also allows for a better test of MODIS C6 data. All fill values from COP and BT data are removed prior to running the VFRTM. The results of the simulation are disappointing and show no correlation to the observed BT values. Upon further analysis

of the data, it seems that a large number of D_{eff} values are set to a value of 0.5 μm which suggests these values were not processed correctly. Upon their removal, a much better result is obtained. To increase the accuracy of the result, all clouds under 4 km were also removed from the data set as these clouds are comprised of water droplets, and the focus of this study is on clouds comprised of ice crystals. The final simulation does very well in comparison to the observed values with RMS error < 4 K for all channels, which represents an error from the VFRTM of $< 1.5\%$ for all cases.

All three tests provide a highly accurate result. The RMS error values are representative of low error from the VFRTM simulations. The highest % error found is in the observations vs. simulations case, and further work can be done to reduce the amount of error. When MERRA data is used for atmospheric profiles and surface temperatures, interpolation between points due to a difference in spatial resolution between data sets is needed. Using reanalysis data is still an improvement upon the use of idealized data sets from previous studies. Reanalysis data is the closest to real time data that can be applied for studies such as this one, and reanalysis data provides a better example of simulation values than idealized data sets. The use of VIIRS data to simulate VIIRS BT values is a big improvement upon previous studies that used other instrumentation data to simulate the observations of VIIRS. Overall, the VFRTM is found to be highly accurate and is validated for further use such as global cloud retrievals to help improve the global energy budget and global climate models.

REFERENCES

Ahrens, C. D., and P. Samson, 2011: *Extreme Weather & Climate*. Brooks/Cole CENGAGE Learning, 508 pp.

Atmospheric and Environmental Research, cited 2016: LBLRTM Description. [Available online at http://rtweb.aer.com/lblrtm_description.html.].

Baran, A. J., 2009: A review of the light scattering properties of cirrus. *J. Quant. Spectrosc. Radiat. Transfer*, **110**, 1239–1260.

Baran, A. J., and P. N. Francis, 2004: On the radiative properties of cirrus cloud at solar and thermal wavelengths: A test of model consistency using high-resolution airborne radiance measurements. *Quart. J. Roy. Meteor. Soc.*, **130**, 763–778.

Baum, B., P. Yang, S. Nasiri, A. K. Heidinger, A. Heymsfield, and J. Li, 2007: Bulk scattering properties for the remote sensing of ice clouds. Part III: high-resolution spectral models from 100 to 3250 cm^{-1}. *J. Appl. Meteor. Climatol.*, **46**, 423–434.

Baumgardner, D., H. Chepfer, G. B. Raga, and G. L. Kok, 2005: The shapes of very small cirrus particles derived from in situ measurements. *Geophys. Res. Lett.*, **32**, 1–4.

Cao, C., J. Xiong, S. Blonski, Q. Liu, S. Uprety, X. Shao, Y. Bai, and F. Weng, 2013a: Suomi NPP VIIRS sensor data record verification, validation, and long-term performance monitoring. *J. Geophys. Res.: Atmos.*, **118**, 11 664–11 678.

Cao, C., and Coauthors, 2013b: Visible Infrared Imaging Radiometer Suite (VIIRS) Sensor Data Record (SDR) User's Guide, Version 1.2. NOAA Technical Report NESDIS 142, NOAA, Washington, DC, 43 pp. [Avilable online at http://www.star.nesdis.noaa.gov/smcd/spb/nsun/snpp/VIIRS/VIIRS_SDR_Users_guide.pdf.].

Chandrasekhar, S., 1960: *Radiative Transfer*. Dover Publications, Inc., 393 pp.

Clough, S. A., F. X. Kneizys, and R. W. Davies, 1989: Line shape and the water vapor continuum. *Atmos. Res.*, **23**, 229–241.

Clough, S. A., F. X. Kneizys, L. S. Rothman, and W. O. Gallery, 1981: Atmospheric spectral transmittance and radiance: FASCOD1B. *Atmos. Transm.*, **277**, 152–166.

Clough, S. A., M. W. Shephard, E. J. Mlawer, J. S. Delamere, M. J. Iacono, K. Cady-Pereira, S. Boukabara, and P. D. Brown, 2005: Atmospheric radiative transfer modeling: a summary of the AER codes. *J. Quant. Spectrosc. Radiat. Transfer*, **91**, 233–244.

Coakley, J., and P. Yang, 2014: *Atmospheric Radiation: A Primer with Illustrative Solutions*. Wiley-VCH, 239 pp.

Cole, B. H., 2013: Global distribution of ice cloud particle shape and roughness from parasol satellite measurements. Ph.D. thesis, Texas A&M University, 102 pp.

Ding, S., P. Yang, F. Weng, Q. Liu, Y. Han, P. van Delst, J. Li, and B. Baum, 2011: Validation of the community radiative transfer model. *J. Quant. Spectrosc. Radiat. Transfer*, **112**, 1050–1064.

Dubuisson, P., V. Giraud, O. Chomette, H. Chepfer, and J. Pelon, 2005: Fast radiative transfer modeling for infrared imaging radiometry. *J. Quant. Spectrosc. Radiat. Transfer*, **95**, 201–220.

Fu, Q., and K. N. Liou, 1993: Parameterization of the radiative properties of cirrus clouds. *J. Atmos. Sci.*, **50**, 2008–2025.

Glickman, T. S., 2000: *Glossary of Meteorology*. American Meteorological Society, 855 pp.

Global Modeling and Assimilation Office, 2012: File Specification for MERRA Products. [Available online at http://gmao.gsfc.nasa.gov/products/documents/MERRA_File_Specification.pdf.].

Heidinger, A. K., C. O'Dell, R. Bennartz, and T. Greenwald, 2006: The successive-order-of-interaction radiative transfer model. Part I: model development. *J. Appl. Meteor. Climatol.*, **45**, 1388–1402.

Hillger, D., cited 2016: VIIRS bands and bandwidths. [Available online at http://rammb.cira.colostate.edu/projects/npp/VIIRS_bands_and_bandwidths.pdf.].

Hillger, D., and Coauthors, 2013: First-light imagery from Suomi NPP VIIRS. *Bull. Amer. Meteor. Soc.*, **94**, 1019–1029.

Hobbs, P. V., L. F. Radke, and D. G. Atkinson, 1975: Airborne measurements and observations in cirrus clouds. Air Force Cambridge Research Laboratories Technical Re-

port 1, University of Washington, Seattle, Washington, 117 pp. [Available online at http://carg.atmos.washington.edu/sys/research/archive/cirrus_clouds_rp1.pdf.].

Holz, R. E., and Coauthors, 2015: Resolving ice cloud optical thickness biases between CALIOP and MODIS using infrared retrievals. *Atmos. Chem. Phys.*, **15**, 29 455–29 495.

Hutchison, K. D., and A. P. Cracknell, 2005: *Visible Infrared Imager Radiometer Suite: A New Operational Cloud Imager*. CRC Press Taylor and Francis Group, 230 pp.

Lahti, C., cited 2016: The Heat Is On - An explanation of how far-infrared heat works. [Available online at http://www.finnleo.com/blog/2011/5/10/the-heat-is-on---an-explanation-of-how-far-infrared-heat-works---by-craig-lahti.aspx.].

Liou, K.-N., 1973: Transfer of solar irradiance through cirrus cloud layers. *J. Geophys. Res.*, **78**, 1409–1418.

Liou, K.-N., 1986: REVIEW influence of cirrus clouds on weather and climate processes: a global perspective. *Mon. Wea. Rev.*, **114**, 1167–1199.

Liou, K.-N., and Y. Takano, 1993: Inference of cirrus cloud properties using satellite-observed visible and infrared radiances. Part I: parameterization of radiance fields. *J. Atmos. Sci.*, **50**, 1279–1304.

Liu, C., P. Yang, S. Nasiri, S. Platnick, K. G. Meyer, C. Wang, and S. Ding, 2014: A fast

Visible Infrared Imaging Radiometer Suite simulator for cloudy atmospheres. *J. Geophys. Res.: Atmos.*, **120**, 240–255.

Magono, C., and C. W. Lee, 1966: Meteorological classification of natural snow crystals. *J. Fac. of Sci., Hokkaido Univ.*, **2**, 321–335.

Meyer, K. G., 2004: The study of cirrus clouds using airborne and satellite data. M.S. thesis, Dept. of Atmospheric Sciences, Texas A&M University, 82 pp.

Nakaya, U., 1954: *Snow Crystals. Natural and Artificial*. Harvard University Press, 510 pp.

NASA, 2011: NPOESS Preparatory Project (NPP) Building a Bridge to a New Era of Earth Observations. NASAfacts, NASA, Greenbelt, MD, 2 pp. [Available online at http://npp.gsfc.nasa.gov/images/npp{%}20factsheet_final.pdf.].

NASA, cited 2016a: About Suomi NPP. [Available online at http://npp.gsfc.nasa.gov/suomi_mission_details.html.].

NASA, cited 2016b: MERRA: Modern Era-Retrospective Analysis for Research and Applications. [Available online at http://gmao.gsfc.nasa.gov/research/merra/intro.php.].

Niu, J., P. Yang, H. L. Huang, J. E. Davies, J. Li, B. A. Baum, and Y. X. Hu, 2007: A fast infrared radiative transfer model for overlapping clouds. *J. Quant. Spectrosc. Radiat. Transfer*, **103**, 447–459.

NOAA, cited 2016: Search VIIRS_SDR. [Available online at http://www.class.ncdc.noaa.gov/saa/products/welcome.].

NOAA NESDIS JPSS, cited 2016: About JPSS Satellites. [Available online at http://www.jpss.noaa.gov/satellites.html.].

Petty, G. W., 2006: *A First Course in Atmospheric Radiation*. Sundog Publishing, 458 pp.

Platnick, S., and X. Xio, 2014: MODIS Atmosphere Team Webinar Overview of Collection 6 Atmosphere and Level-1B Calibration. [Available online at http://modis-atmos.gsfc.nasa.gov/Webinar2014/MODISAtmWebinar1Platnick.pdf.].

Platnick, S., and Coauthors, 2015: MODIS cloud optical properties: User guide for the Collection 6 Level-2 MOD06/MYD06 product and associated Level-3 Datasets. [Available online at http://modis-atmos.gsfc.nasa.gov/_docs/C6MOD06OPUserGuide.pdf.].

Raytheon Company, 2011: Visible/Infrared Imager Radiometer Suite (VIIRS). Tech. rep., Raytheon, El Segundo, CA, 2 pp. [Available online at http://npp.gsfc.nasa.gov/images/viirs_ds152{%}20approved{%}208-10-11.pdf.].

Seaman, C., 2013: Beginner's Guide to VIIRS Imagery Data. [Available online at http://rammb.cira.colostate.edu/projects/npp/Beginner_Guide_to_VIIRS_Imagery_Data.pdf.].

Seaman, C., D. Hillger, T. Kopp, R. Williams, S. Miller, and D. Lindsey, 2014: Visible Infrared Imaging Radiometer Suite (VIIRS), Imagery Environmental Data Record

(EDR) User's Guide, Version 1.1. NOAA Technical Report, NOAA, Washington, DC, 40 pp. [Available online at http://rammb.cira.colostate.edu/projects/npp/VIIRS_Imagery_EDR_Users_Guide.pdf.].

SSEC University of Wisconsin-Madison, 2012: Suomi NPP Instrument Packages Already Hard at Work. [Available online at http://www.ssec.wisc.edu/news/articles/104.].

Stamnes, K., S. Tsay, W. Wiscombe, S. Freidenreich, I. Laszlo, R. Song, and R. Pincus, 2000: A Discrete Ordinates Radiative Transfer Fortran-90 Program for a Multi-Layered Plane-Parallel Medium (Version 2.0). Documentation File for 'DISORT', NASA. [Available online at ftp://climate.gsfc.nasa.gov/pub/wiscombe/Multiple_Scatt/.].

Stamnes, K., S. Tsay, W. Wiscombe, and K. Jayaweera, 1988: Numerically stable algorithm for discrete-ordinate-method radiative transfer in multiple scattering and emitting layered media. *J. Opt. Soc. Amer.*, **27**, 2502–2509.

Stephens, G. L., and Coauthors, 2012: An update on earth's energy balance in light of the latest global observations. *Nat. Geosci.*, **5**, 691–696.

Stubenrauch, C. J., and Coauthors, 2013: Assessment of global cloud datasets from satellites. *Bull. Amer. Meteor. Soc.*, 1031–1049.

Trenberth, K. E., J. T. Fasullo, and J. Kiehl, 2009: Earth's global energy budget. *Bull. Amer. Meteor. Soc.*, 311–324.

US Navy, cited 2016: Infrared window. [Available online at http://web.archive.org/web/20010913094914/http:/ewhdbks.mugu.navy.mil/transmit.gif.].

Wang, C., 2013: Investigation of Thin Cirrus Cloud Optical and Microphysical Properties on the Basis of Satellite Observations and Fast Radiative Transfer Models. Ph.D. thesis, Texas A&M University, 165 pp.

Wang, C., P. Yand, B. A. Baum, S. Platnick, A. K. Heidinger, Y. Hu, and R. E. Holz, 2011: Retrieval of ice cloud optical thickness and effective particle size using a fast infrared radiative transfer model. *J. Appl. Meteor. Climatol.*, **50**, 2283–2297.

Wang, C., P. Yang, S. Platnick, A. K. Heidinger, B. A. Baum, T. Greenwald, Z. Zhang, and R. E. Holz, 2013: Retrieval of ice cloud properties from AIRS and MODIS observations based on a fast high-spectral-resolution radiative transfer model. *J. Appl. Meteor. Climatol.*, **52**, 710–726.

Wei, H., P. Yang, J. Li, B. Baum, H.-L. Huang, S. Platnick, Y. Hu, and L. Strow, 2004: Retrieval of semitransparent ice cloud optical thickness from atmospheric infrared sounder (AIRS) measurements. *IEEE Trans. Geosci. Electron.*, **42**, 2254–2267.

Wendisch, M., and P. Yang, 2012: *Theory of Atmospheric Radiative Transfer*. Wiley-VCH, 321 pp.

Wiscombe, W. J., 1977: The delta-M method: rapid yet accurate radiative flux calculations for strongly asymmetric phase functions. *J. Atmos. Sci.*, **34**, 1408–1422.

Yagi, T., 1969: On the relation between the shape of cirrus clouds and the static stability of cloud level-studies of cirrus clouds: Part iv. *J. Meteor. Soc. Jpn.*, **47**, 59–64.

Yang, P., B.-C. Gao, B. A. Baum, Y. X. Hu, W. J. Wiscombe, S.-C. Tsay, D. M. Winker, and S. L. Nasiri, 2001: Radiative properties of cirrus clouds in the infrared (8-13 μm) spectral region. *J. Quant. Spectrosc. Radiat. Transfer*, **70**, 473–504.

Yang, P., K. N. Liou, L. Bi, C. Liu, B. Yi, and B. A. Baum, 2014: On the radiative properties of ice clouds: light scattering, remote sensing, and radiation parameterization. *Adv. Atmos. Sci.*, **32**, 32–63.

Yang, P., H. Wei, H. L. Huang, B. Baum, Y. X. Hu, G. W. Kattawar, M. I. Mishchenko, and Q. Fu, 2005: Scattering and absorption property database for nonspherical ice particles in the near- through far-infrared spectral region. *App. Opt.*, **44**, 5512–5523.

Zhang, Z., P. Yang, G. W. Kattawar, S. C. Tsay, B. A. Baum, Y. Hu, A. J. Heymsfield, and J. Reichardt, 2004: Geometrical optics solution to light scattering by droxtal ice crystals. *App. Opt.*, **43**, 2490–2499.

Zhang, Z., and Coauthors, 2007: A fast infrared radiative transfer model based on the adding-double method for hyperspectral remote-sensing applications. *J. Quant. Spectrosc. Radiat. Transfer*, **105**, 243–263.

APPENDIX A

SCATTER PLOTS

A.1 Cloudy Sky Examples: June 20, 2014

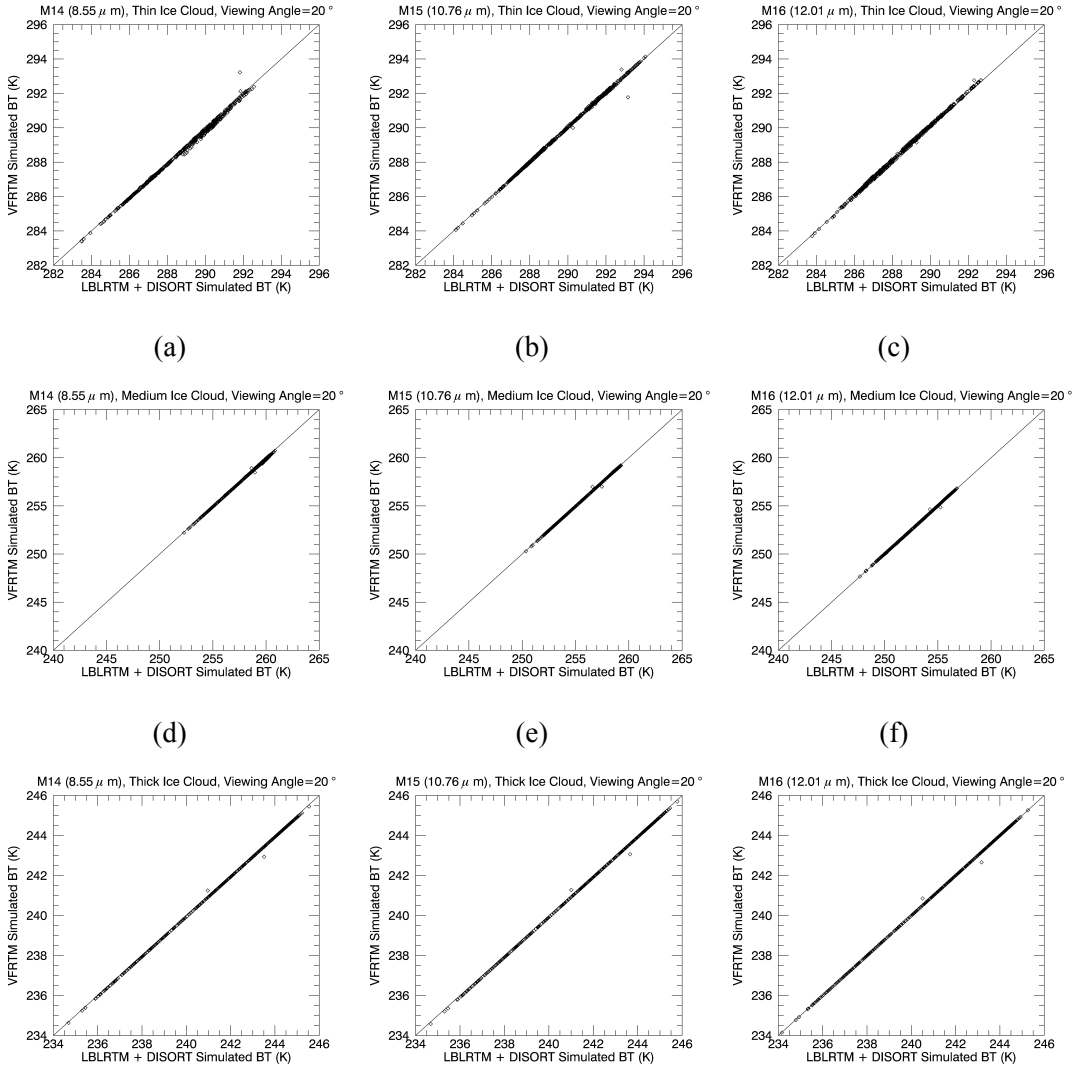

Figure A.1: Cloudy sky examples June 20, 2016 channels M14, M15, and M16: (a)-(c) thin, (d)-(f) medium, (g)-(i) thick

A.2 Additional Satellite Viewing Zenith Angle Examples: June 21, 2014

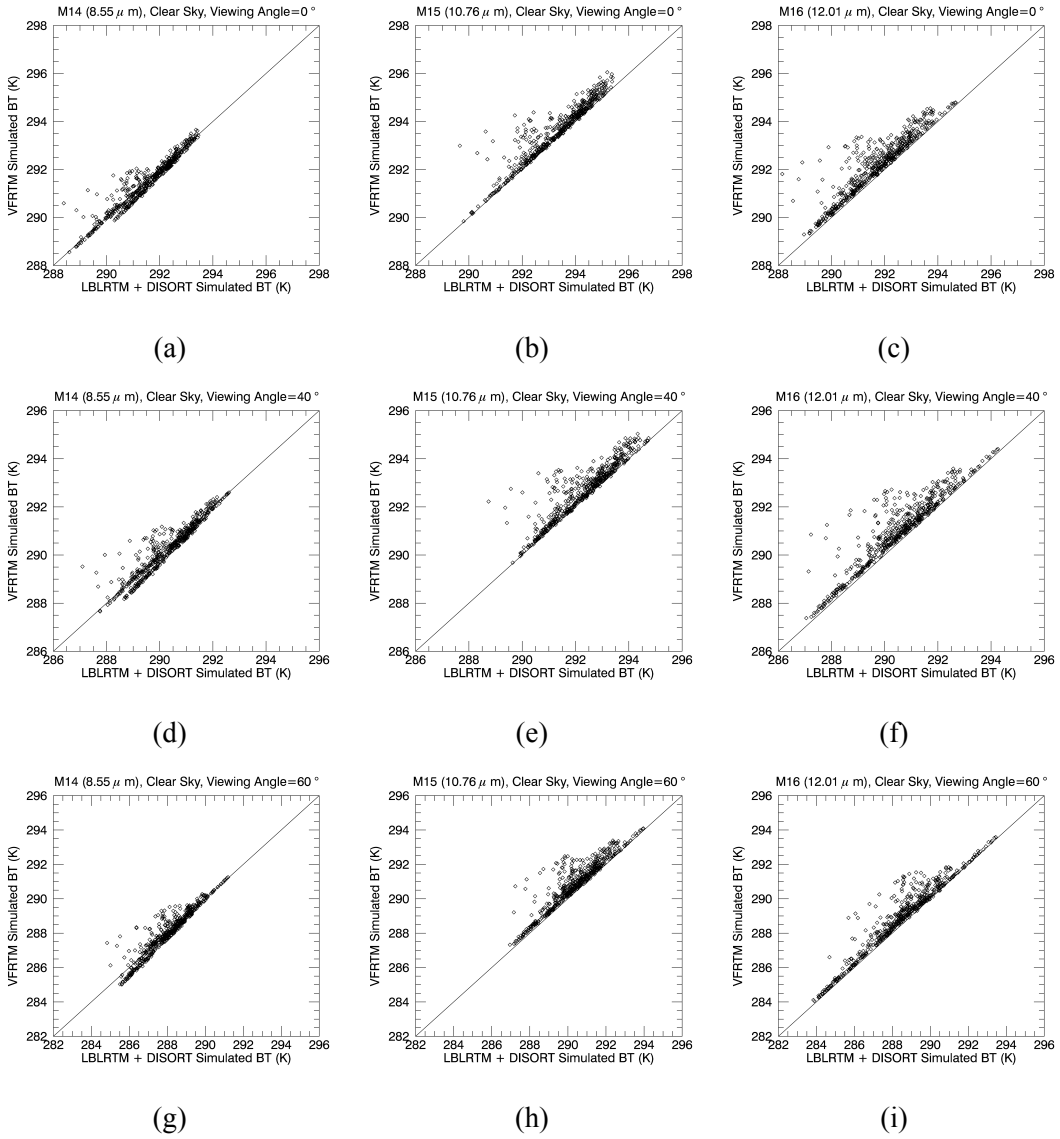

Figure A.2: Clear sky examples channels M14, M15, and M16: (a)-(c) 0°, (d)-(f) 40°, (g)-(i) 60°

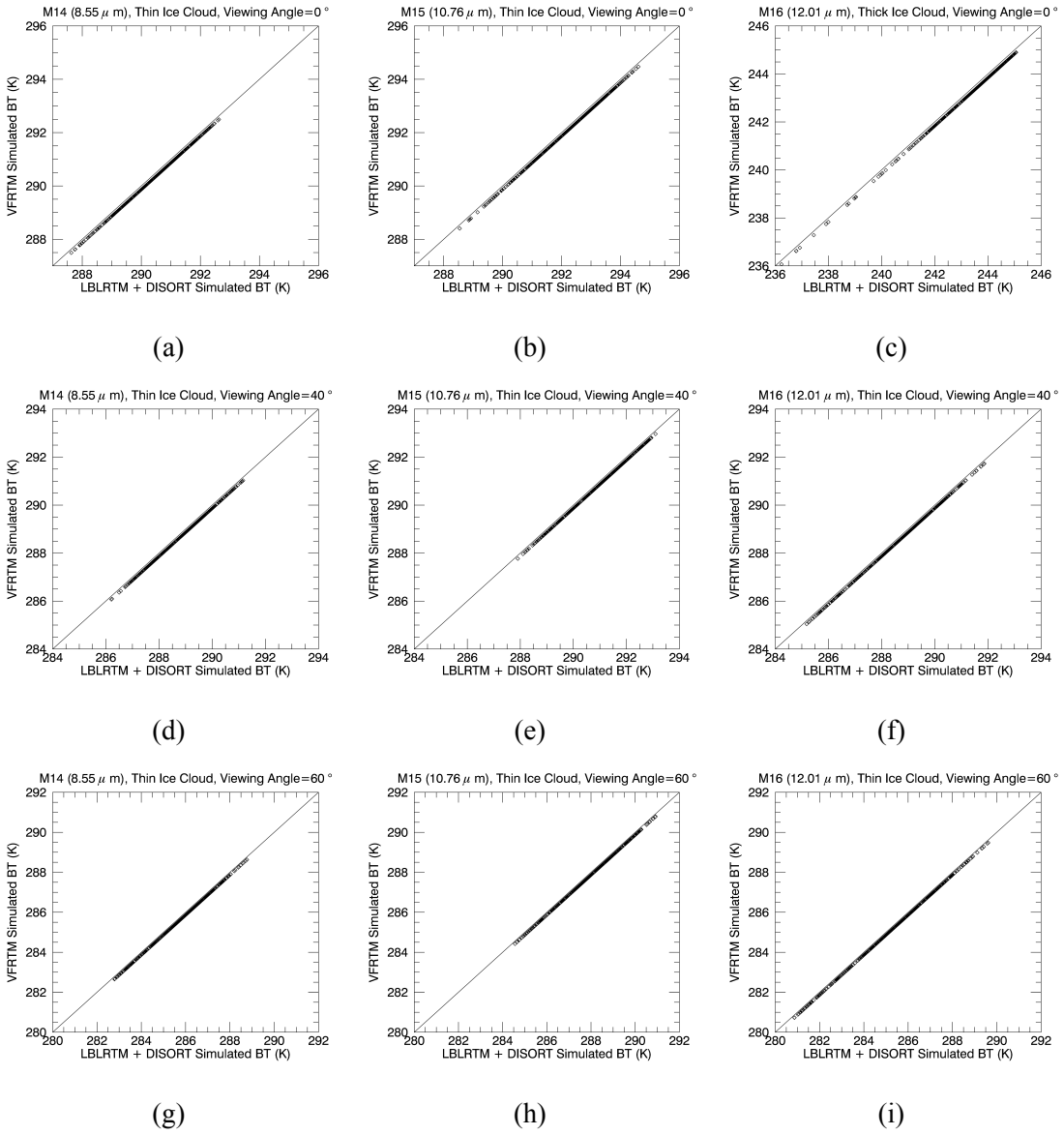

Figure A.3: Thin cloud examples channels M14, M15, and M16: (a)-(c) 0°, (d)-(f) 40°, (g)-(i) 60°

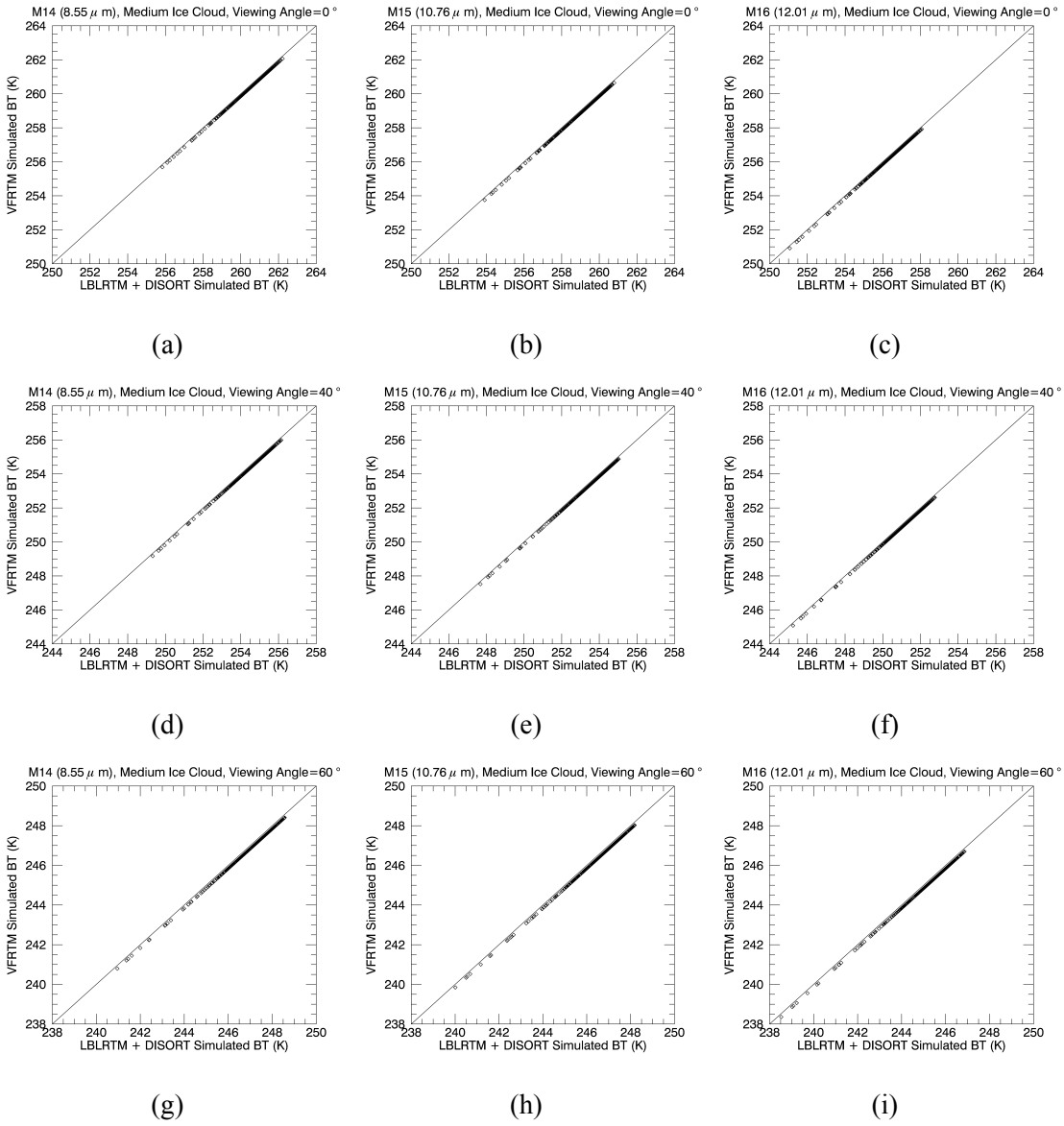

Figure A.4: Medium cloud example channels M14, M15, and M16: (a)-(c) 0°, (d)-(f) 40°, (g)-(i) 60°

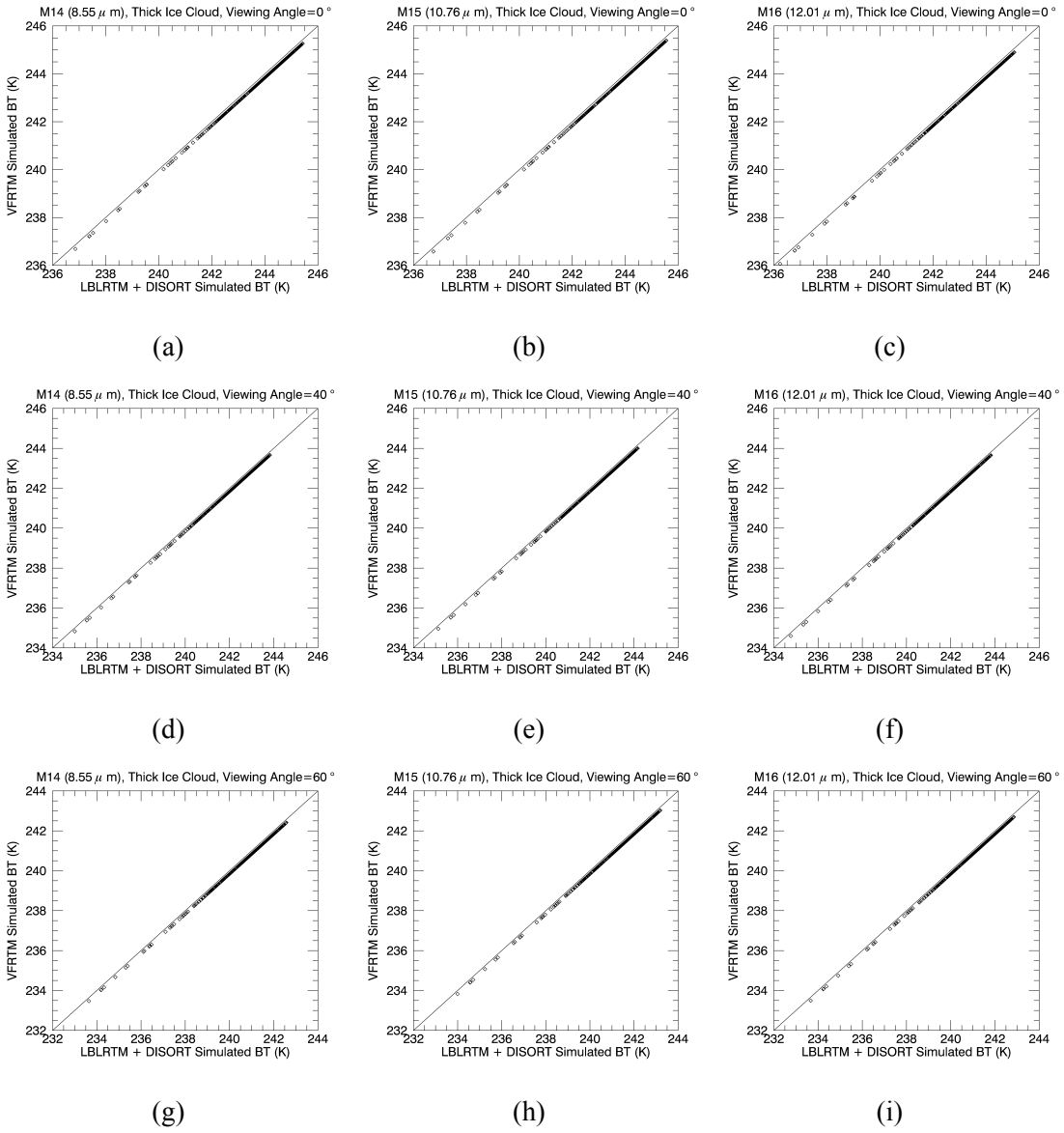

Figure A.5: Thick cloud example channels M14, M15, and M16: (a)-(c) 0°, (d)-(f) 40°, (g)-(i) 60°

APPENDIX B

BTD PLOTS

B.1 Additional Select Pixels: June 20, 2014

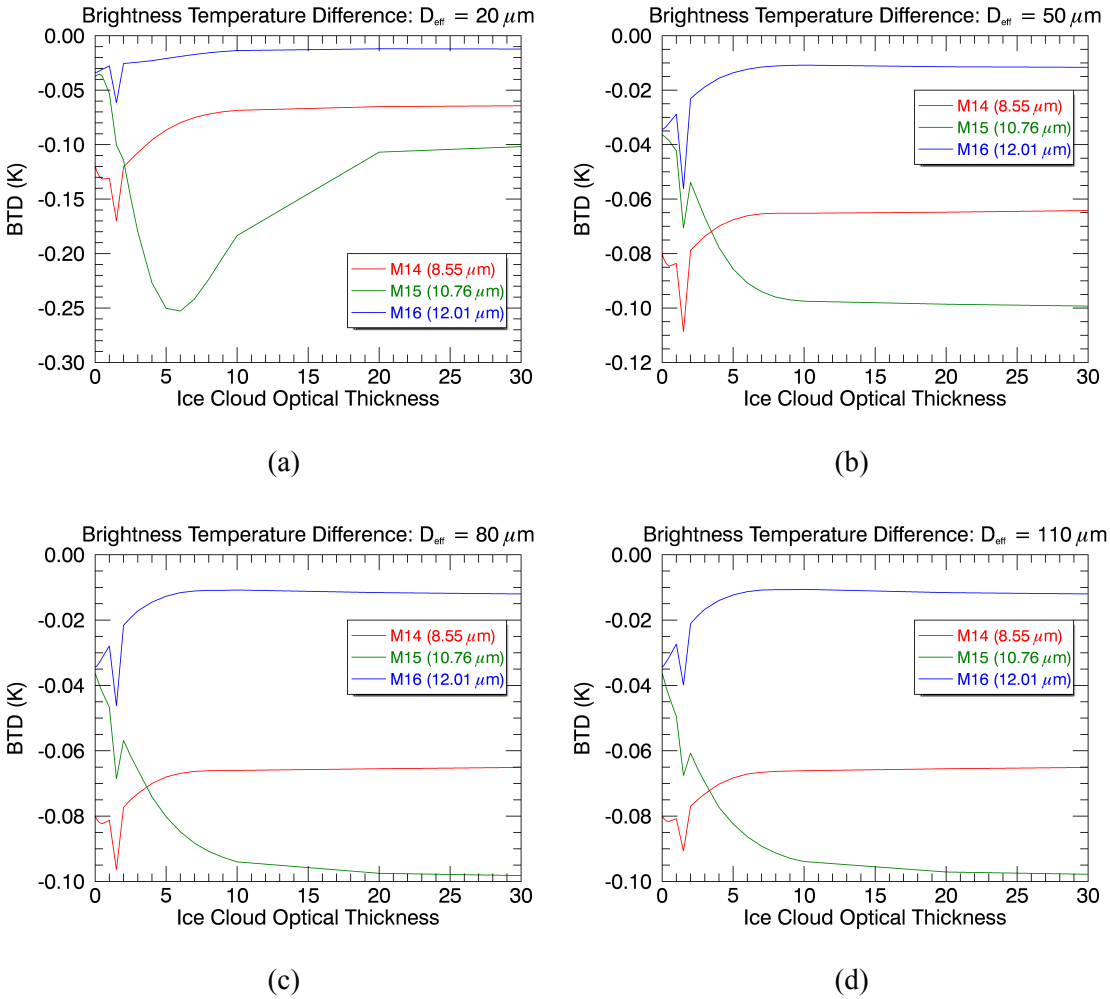

Figure B.1: Brightness temperature difference for 31°N/117°W June 20, 2014

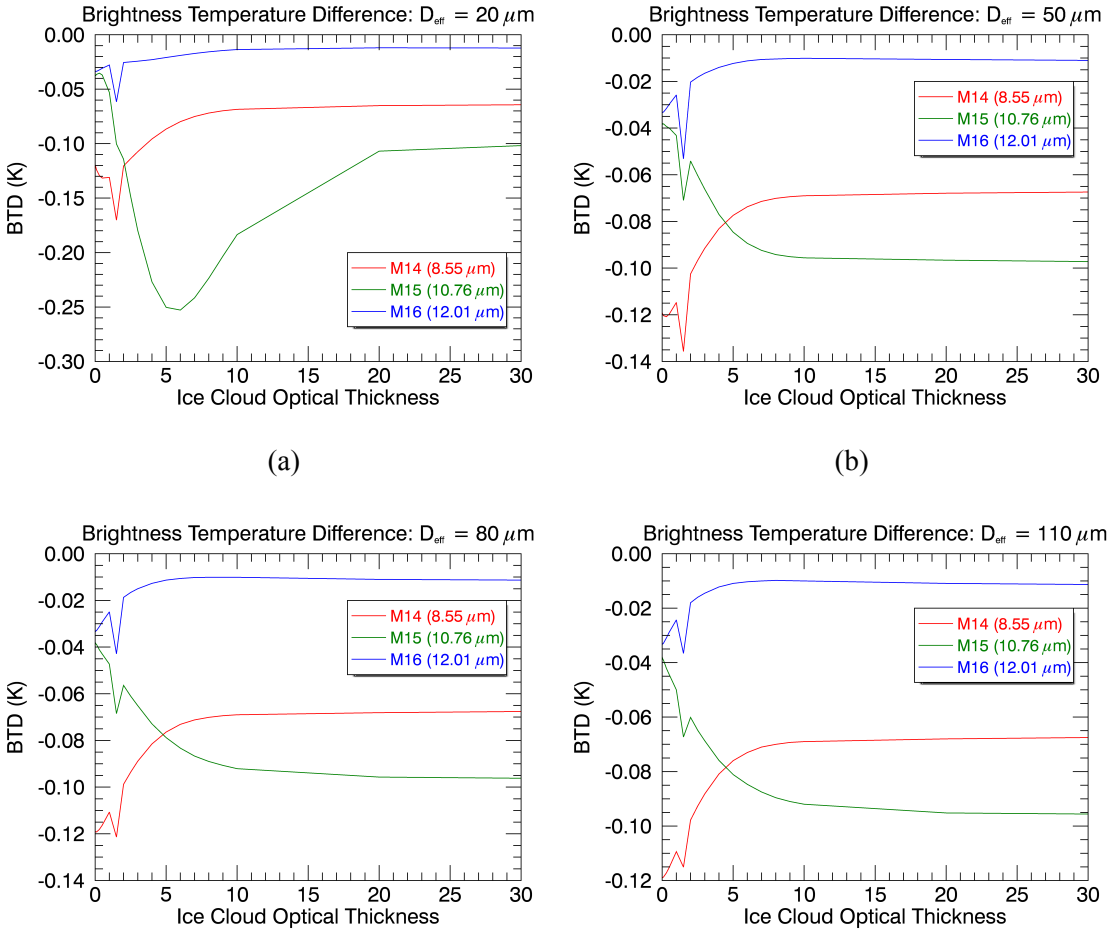

Figure B.2: Brightness temperature difference for 28°N/118°W June 20, 2014

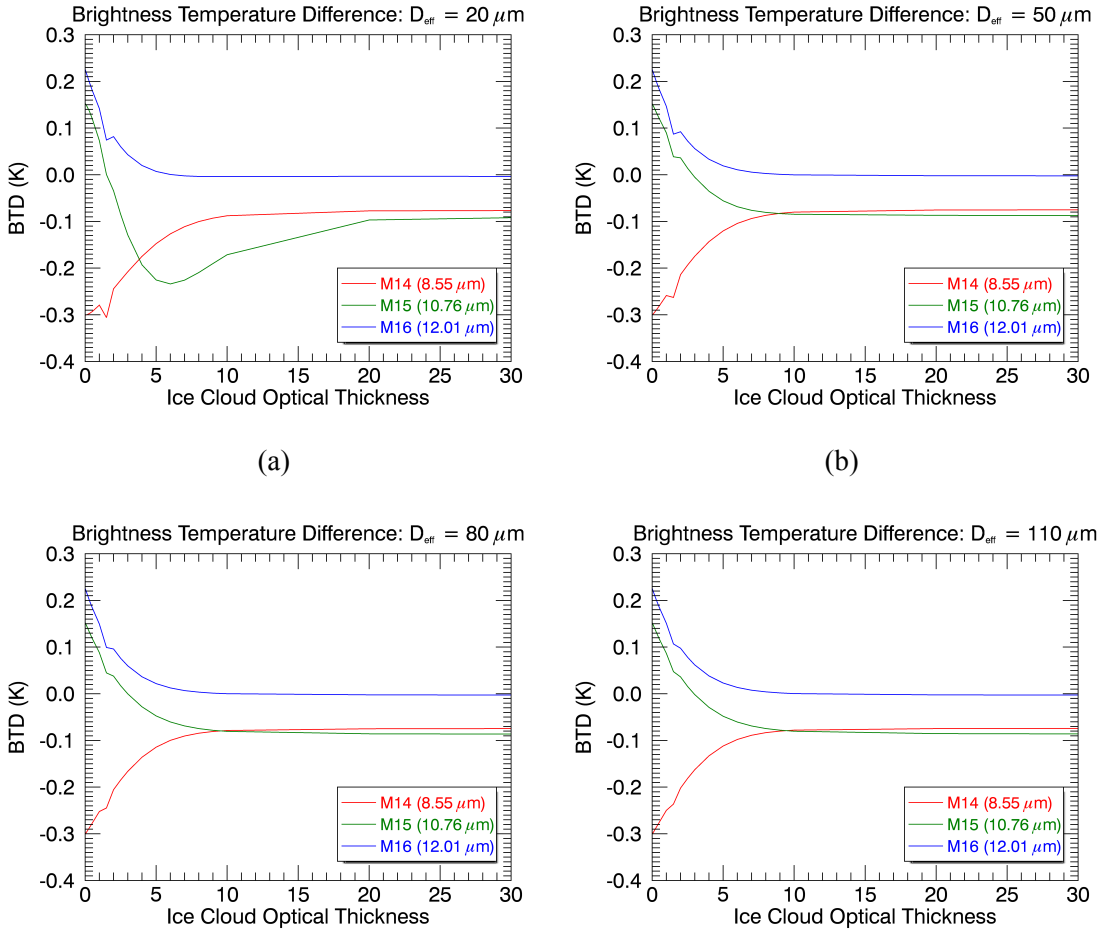

Figure B.3: Brightness temperature difference for 14°N/128°W June 20, 2014

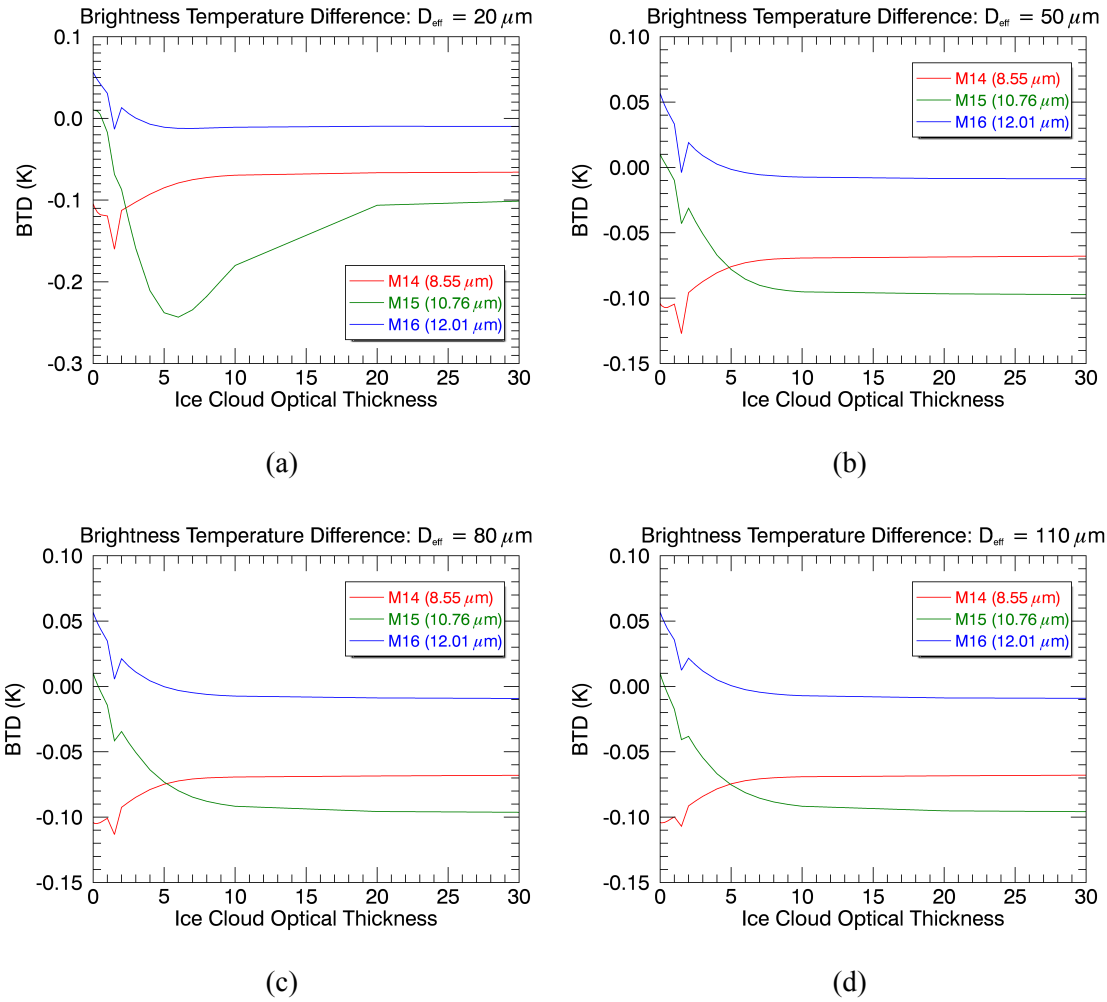

Figure B.4: Brightness temperature difference for 29°N/132°W June 20, 2014

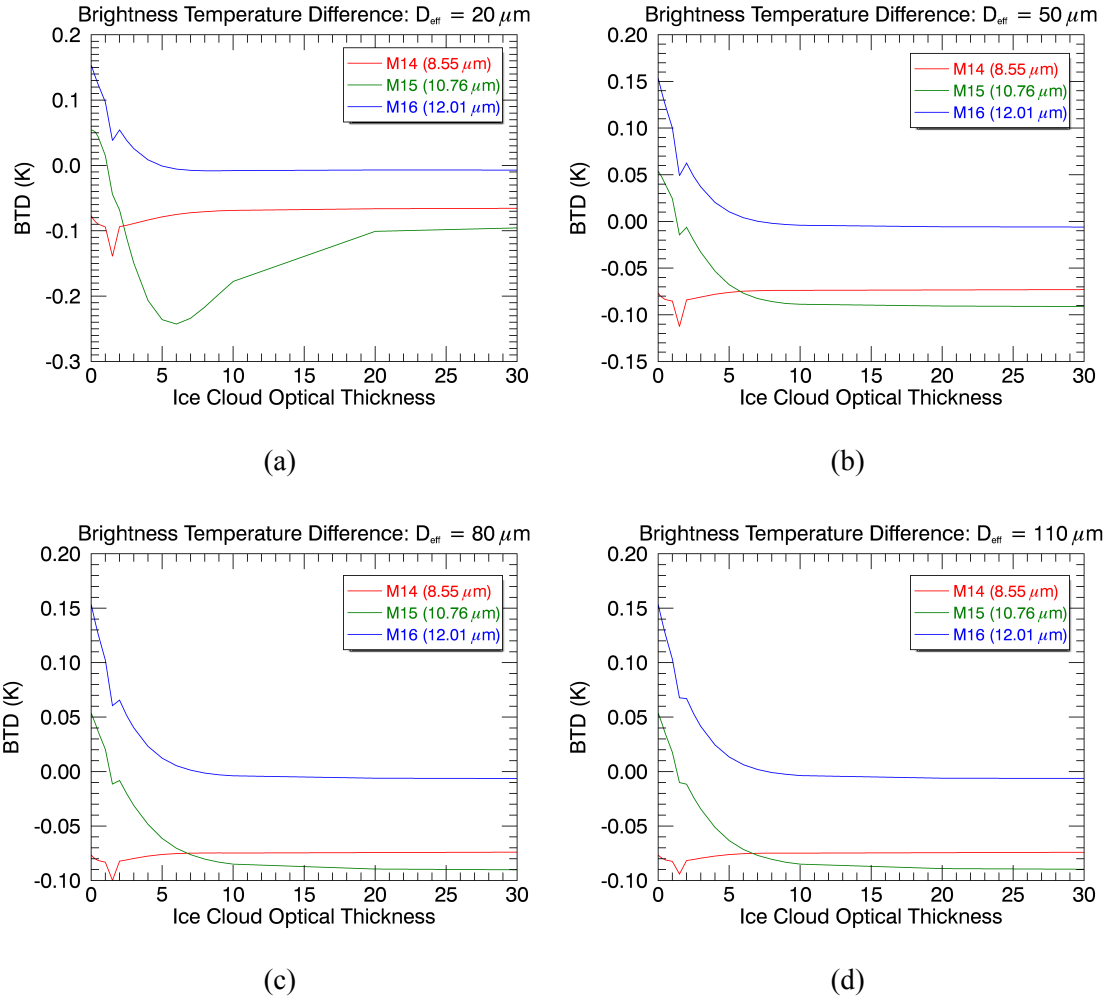

Figure B.5: Brightness temperature difference for 19°N/138°W June 20, 2014

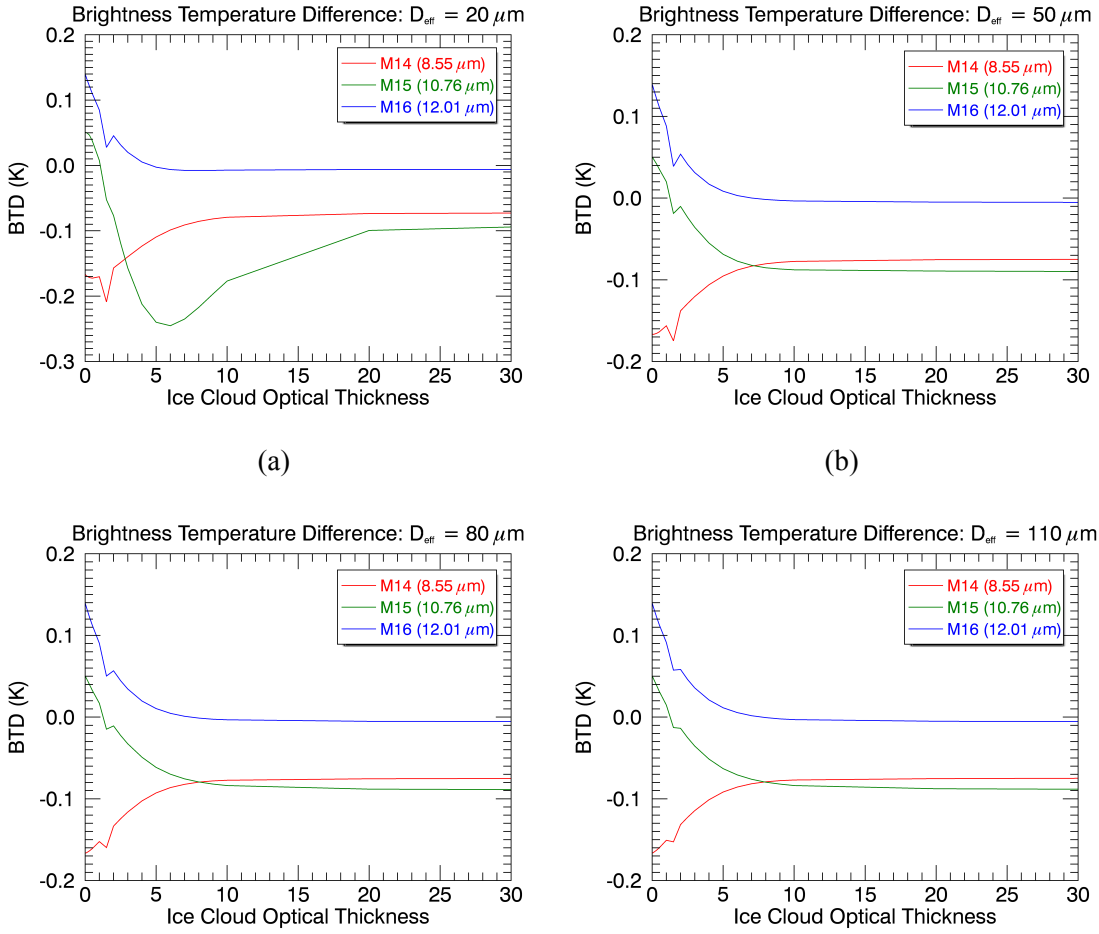

Figure B.6: Brightness temperature difference for 14°N/142°W June 20, 2014

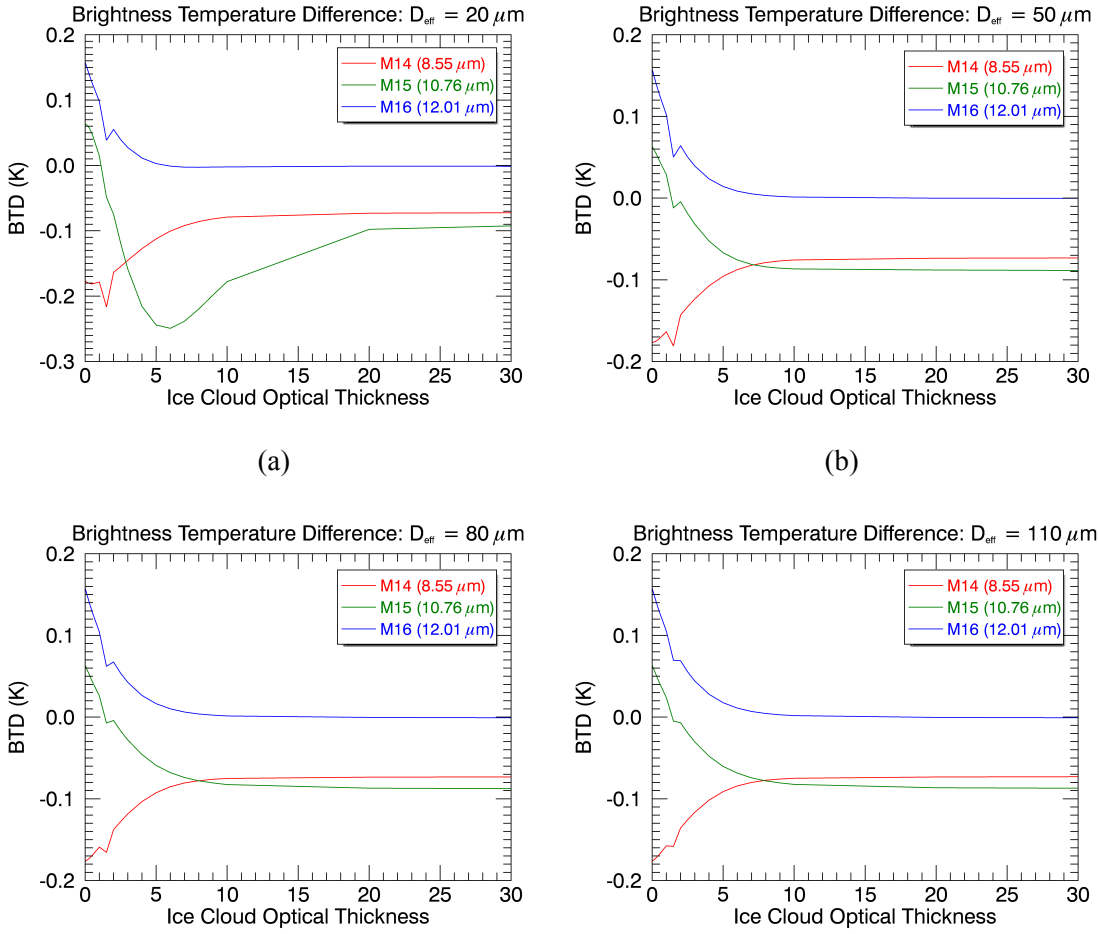

Figure B.7: Brightness temperature difference for 11°N/146°W June 20, 2014

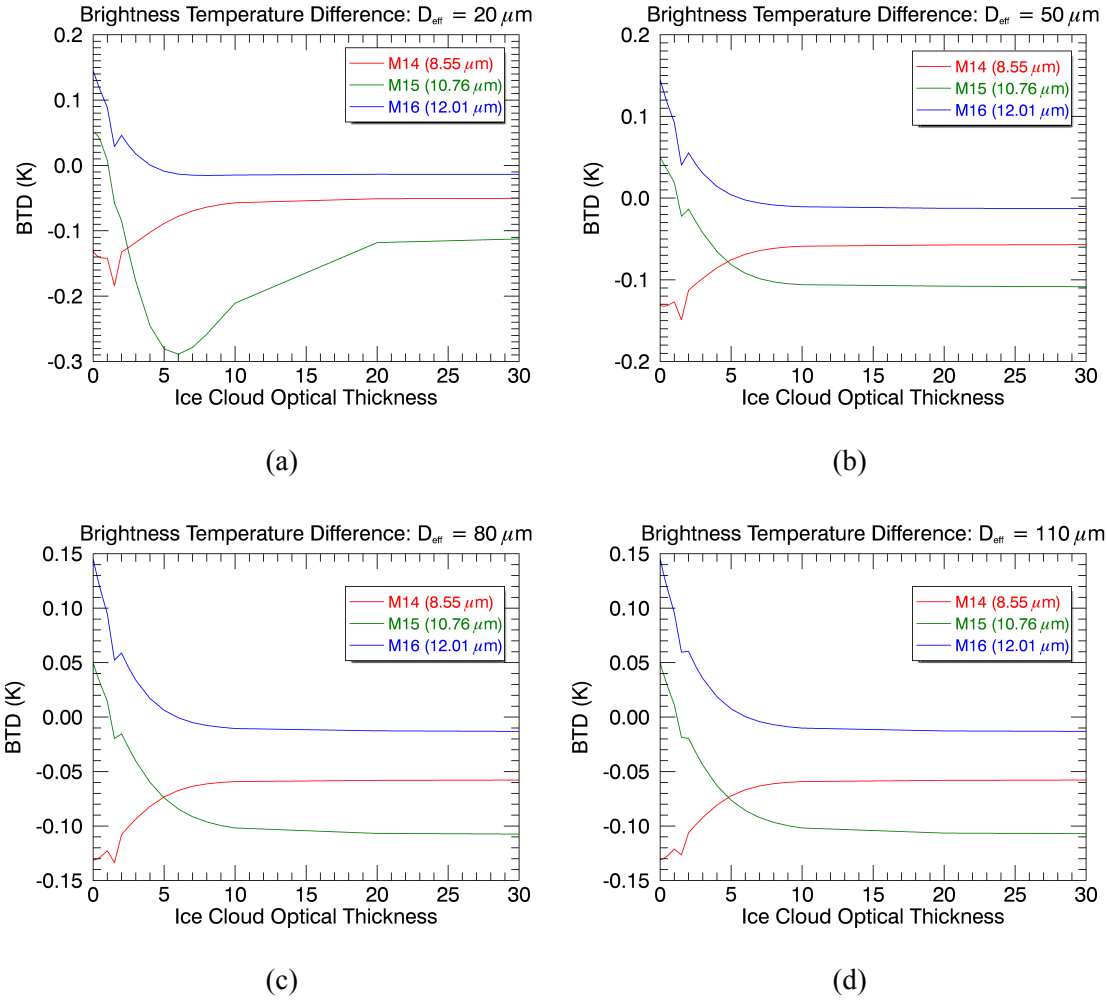

Figure B.8: Brightness temperature difference for 26°N/148°W June 20, 2014

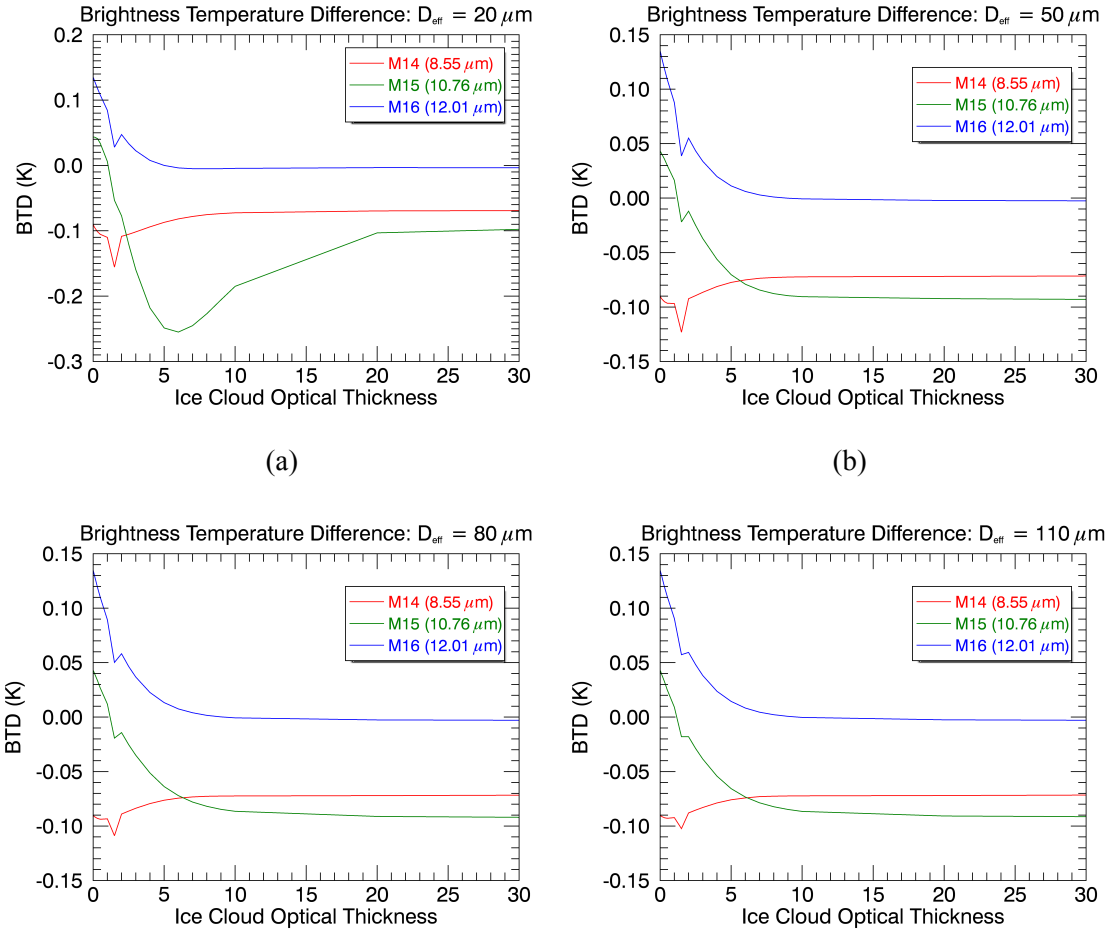

Figure B.9: Brightness temperature difference for 17°N/151°W June 20, 2014

B.2 Additional Select Pixels: June 21, 2014

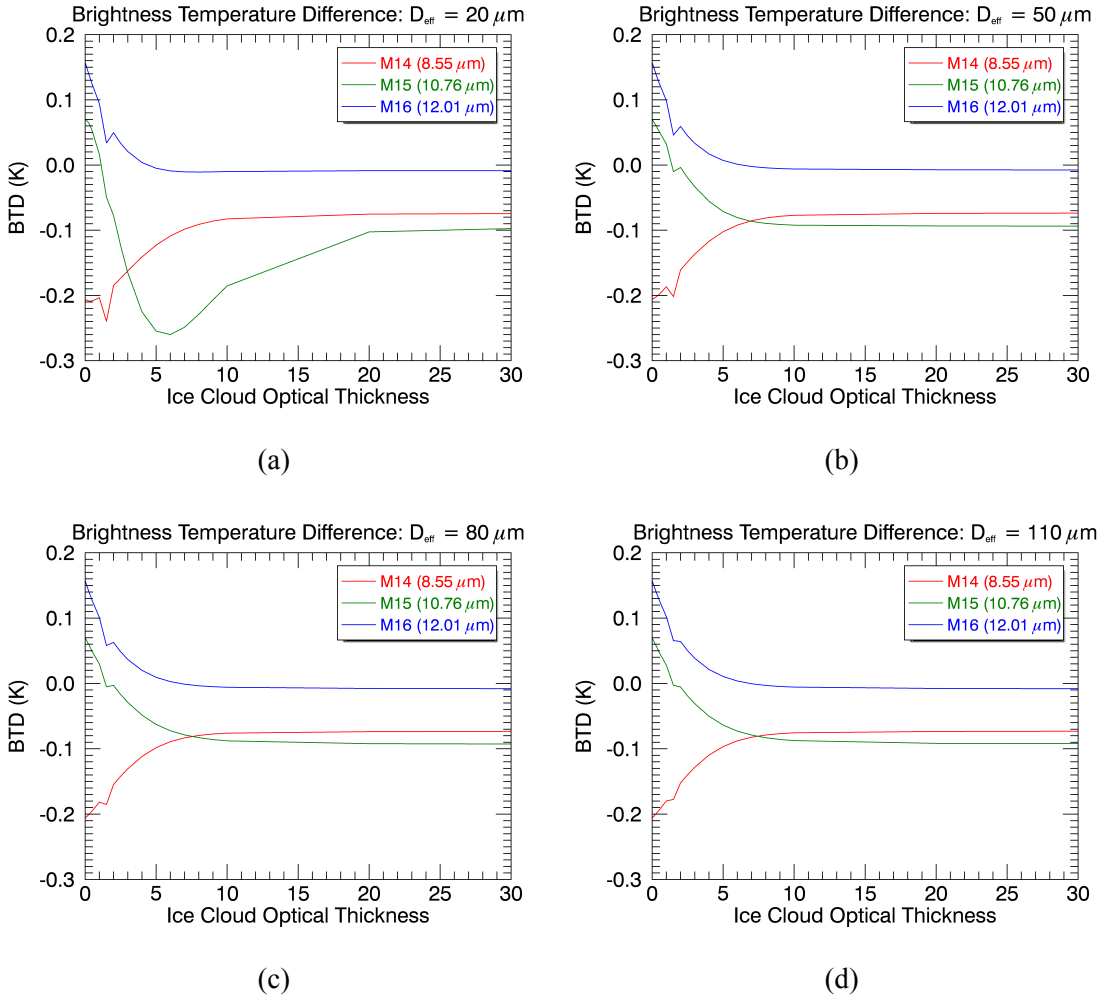

Figure B.10: Brightness temperature difference for 1°N/119°W June 21, 2014

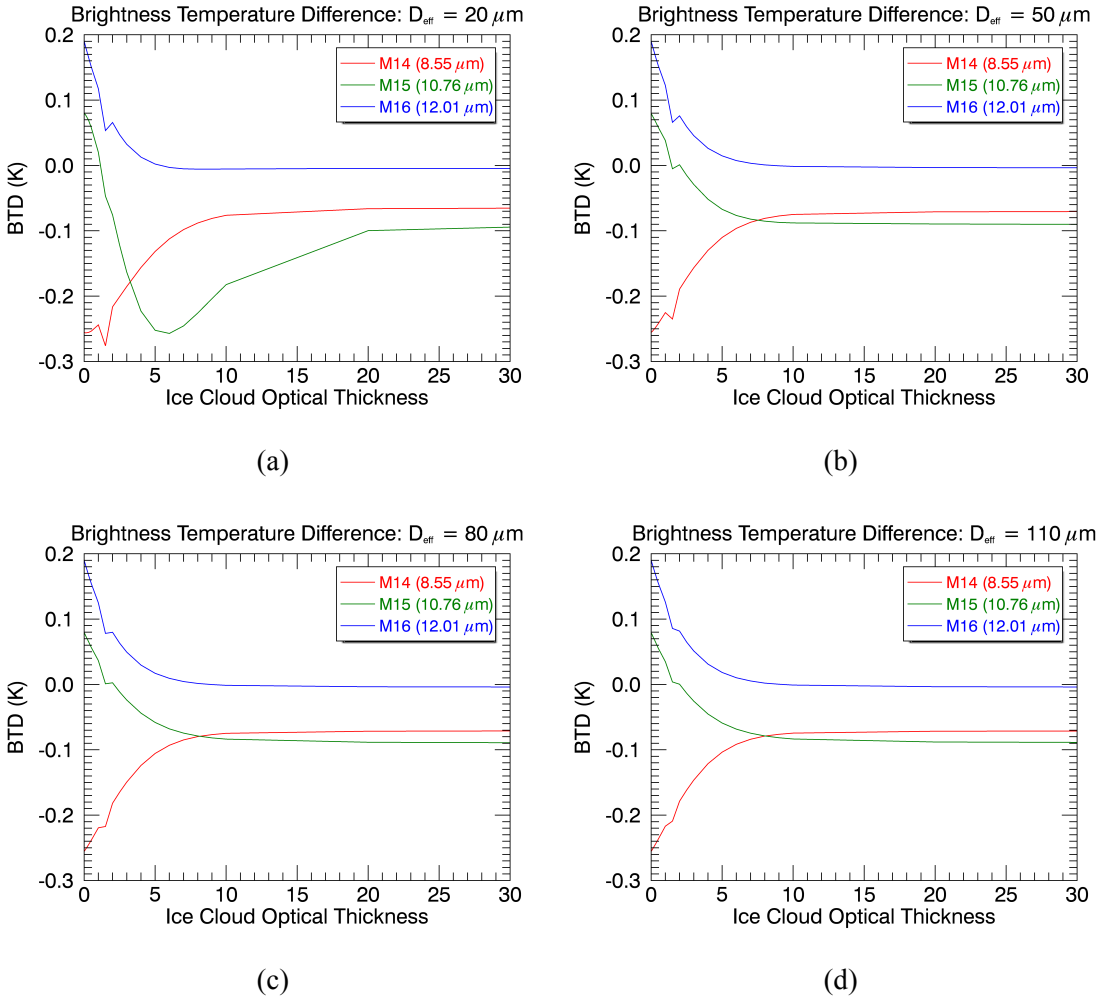

Figure B.11: Brightness temperature difference for 12°N/121°W June 21, 2014

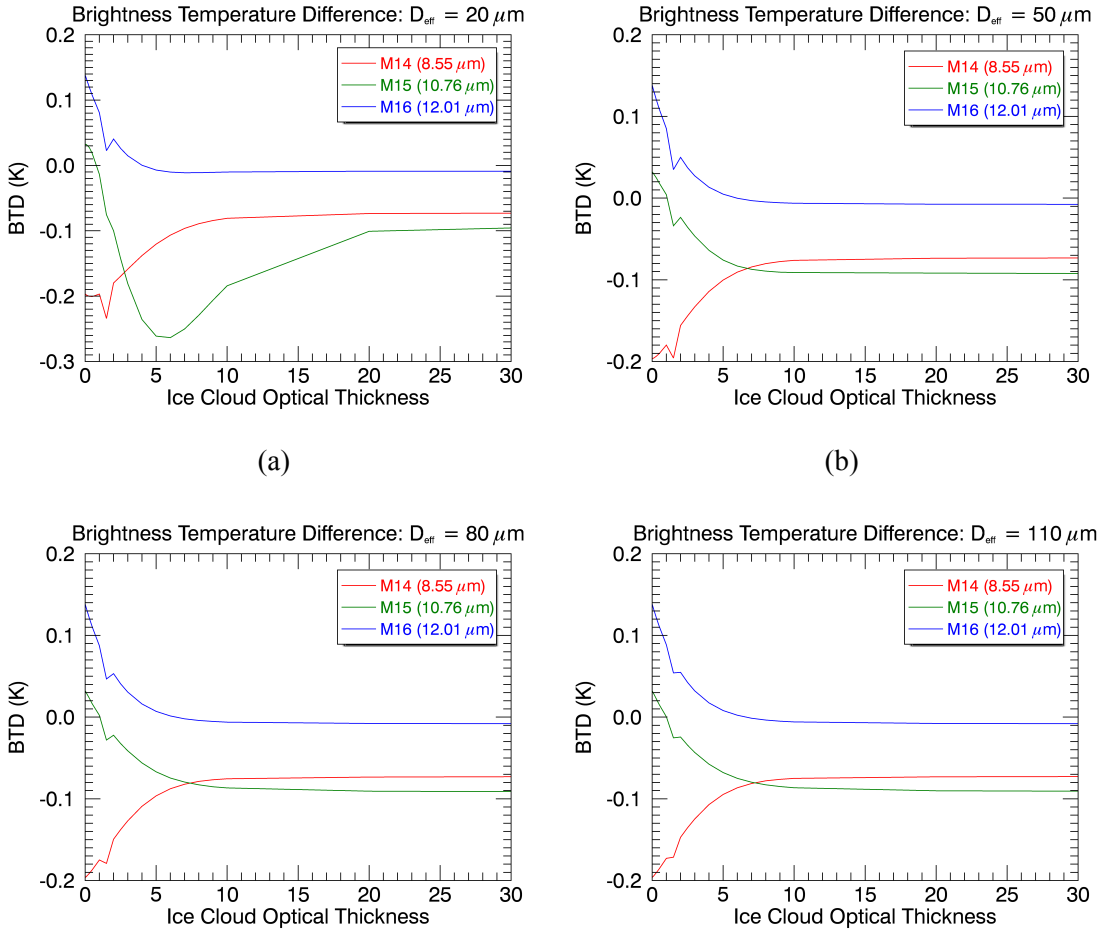

Figure B.12: Brightness temperature difference for 3°N/122°W June 21, 2014

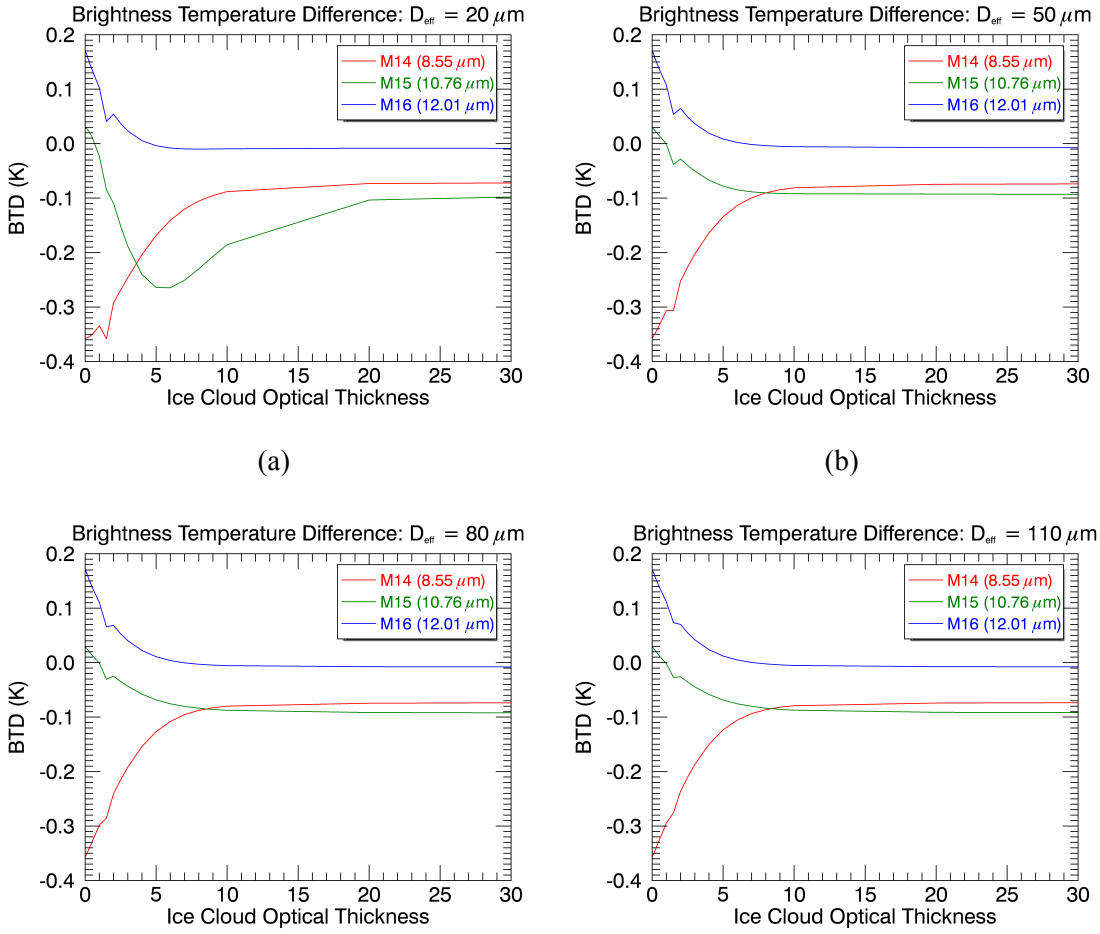

Figure B.13: Brightness temperature difference for 8°N/123°W June 21, 2014

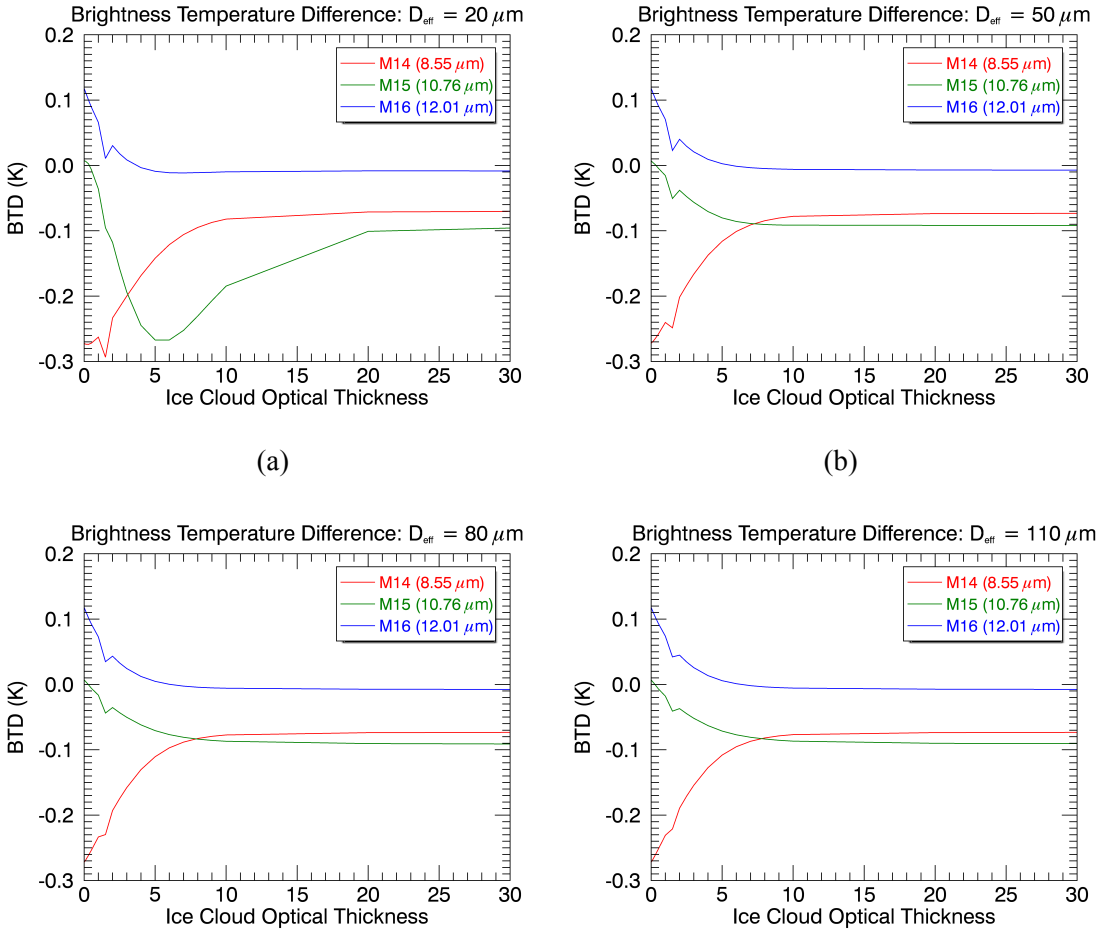

Figure B.14: Brightness temperature difference for 2°N/133°W June 21, 2014

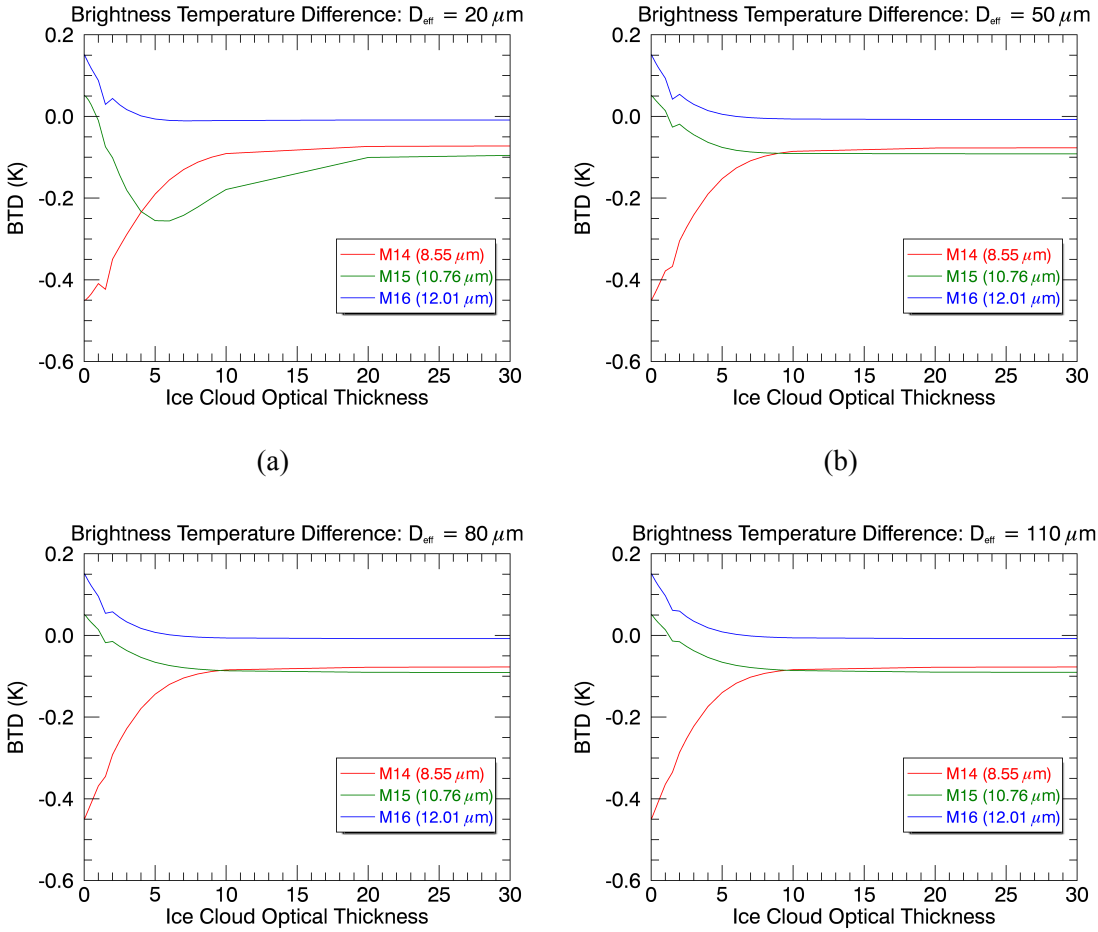

Figure B.15: Brightness temperature difference for 4°N/134°W June 21, 2014

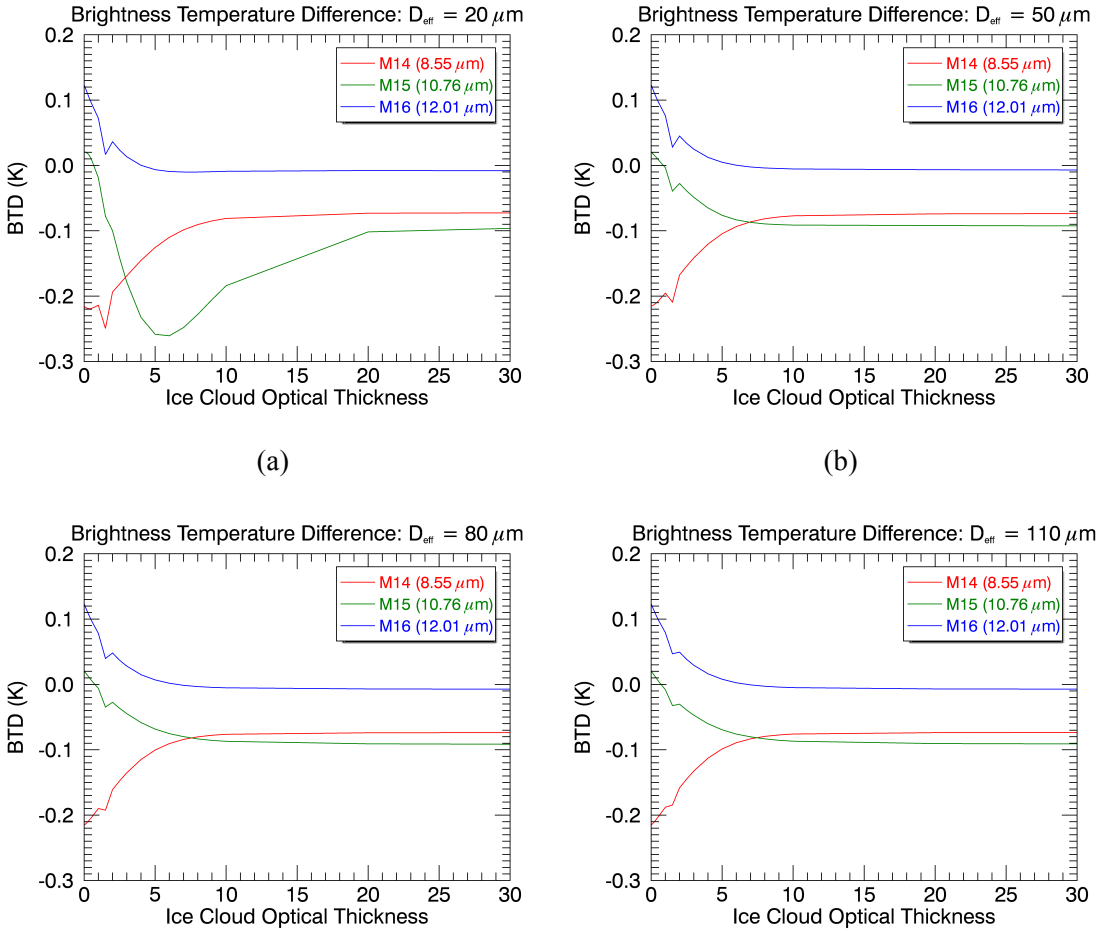

Figure B.16: Brightness temperature difference for 14°N/144°W June 21, 2014

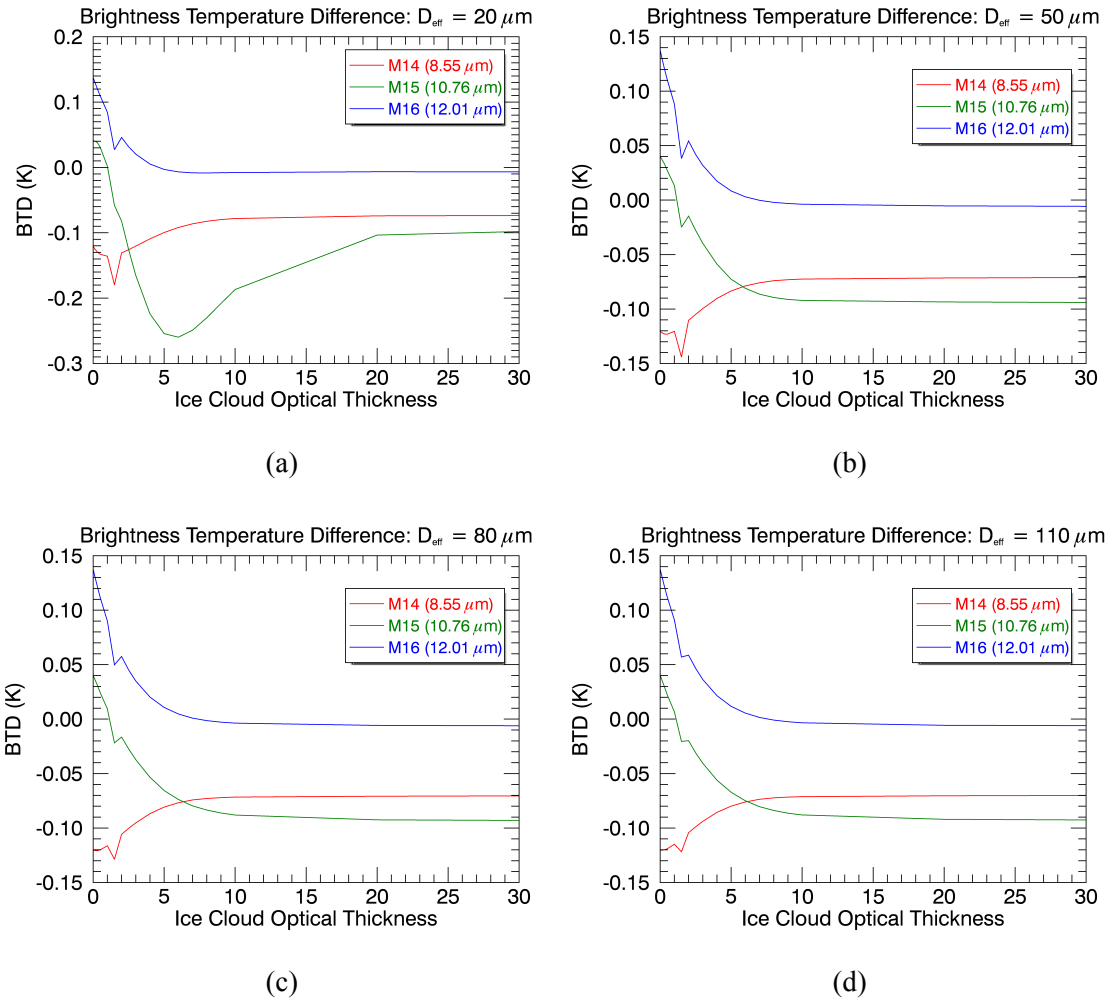

Figure B.17: Brightness temperature difference for 16°N/149°W June 21, 2014

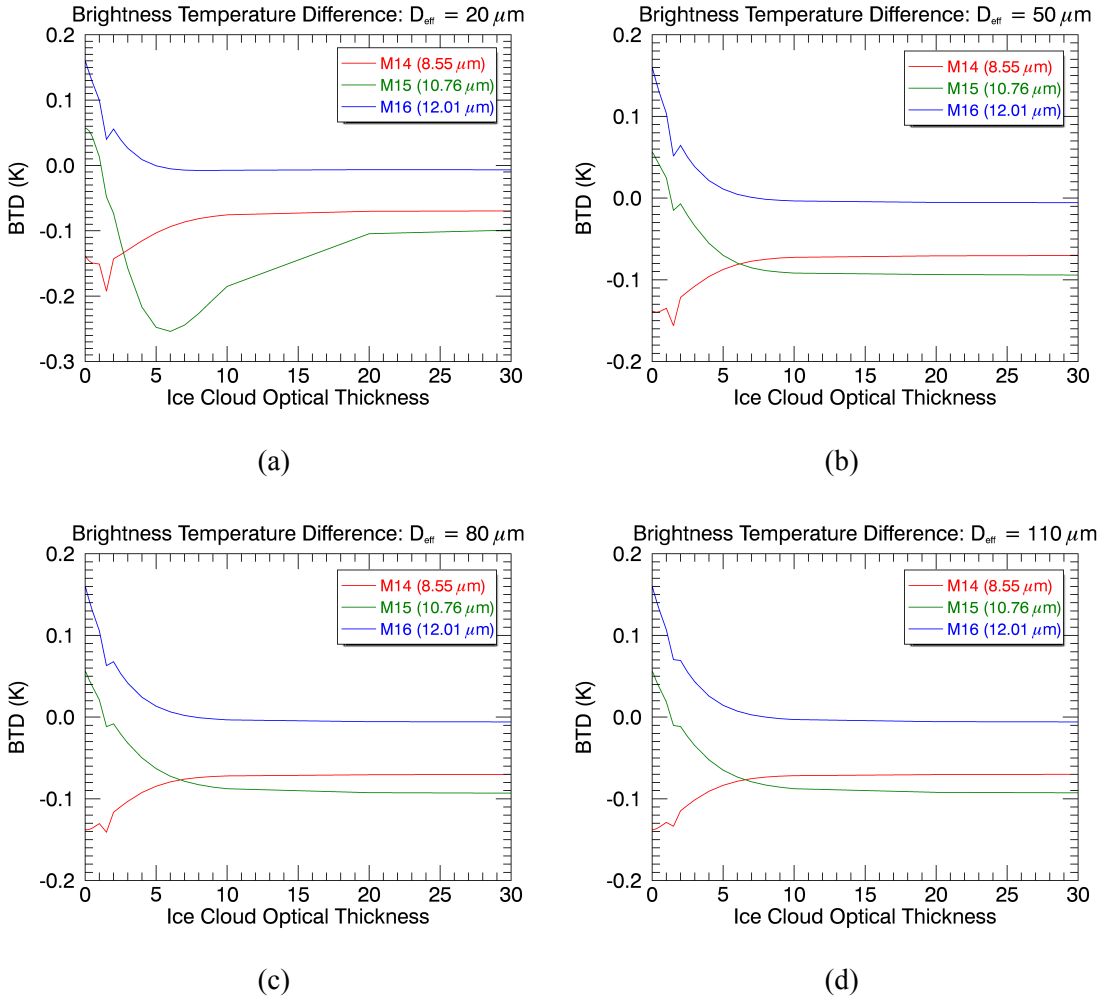

Figure B.18: Brightness temperature difference for 19°N/151°W June 21, 2014